On the O 2 "Surfactant" Effect During Ag/SiO 2 Magnetron Sputtering Deposition: the Point of View of In situ and Real-time Measurements

Ramiro Zapata, Matteo Balestrieri, Iryna Gozhyk, Hervé Montigaud, Rémi Lazzari

On the O_2 "Surfactant" Effect During Ag/SiO_2 Magnetron Sputtering Deposition: the Point of View of *In Situ* and Real-time Measurements

Ramiro Zapata,[†,‡] Matteo Balestrieri,[†] Iryna Gozhyk,[†] Hervé Montigaud,[†] and Rémi Lazzari[*,‡]

†*Surface du Verre et Interfaces, UMR 125 CNRS/Saint-Gobain Recherche, 39 Quai Lucien Lefranc BP 135, F-93303 Aubervilliers, France*
‡*CNRS, Sorbonne Université, Institut des NanoSciences de Paris, UMR 7588, 4 Place Jussieu, F-75005 Paris, France*

E-mail: remi.lazzari@insp.jussieu.fr

Abstract

The use of gaseous species has been proposed in the literature to counteract the three-dimensional growth tendency of noble metals on dielectric substrates and favour an earlier percolation without compromising electrical properties. This "surfactant" effect is rationalized herein in the case of O_2 presence during magnetron sputtering deposition of Ag films on SiO_2. *In situ* and real-time techniques (X-ray photoemission, film resistivity, UV-visible optical spectroscopy) and *ex situ* characterizations (x-ray diffraction and transmission electron microscopy) were combined to scrutinize the impact of O_2 addition in the gas flow ($\%O_2$), revealing three regimes of evolution of film resistivity, morphology, structure and chemical composition. At low oxygen flow conditions ($\%O_2 < 4$), the observed drastic decrease of the percolation threshold is assigned to a combination of (i) a change in nanoparticle density, wetting and crystallographic texture and (ii) of a delayed coalescence effect. The driving force is ascribed to the presence of specific adsorbed oxygen moieties, the nature of which starts evolving at intermediate oxygen flow conditions ($10 \leq \%O_2 < 20$). At high oxygen flow ($20 \leq \%O_2 < 40$), the found detrimental impact on film resistivity is assigned to an actual oxidation in the form of an Ag_2O-like poorly crystallized compound. For all $\%O_2$, a composition gradient is observed across the film thickness, with a more metallic Ag at the substrate interface. A correlation between percolation and the nature of the detected O moities is observed. In parallel to an oxygen spillover mechanism, this gradient can be explained by the competition between different surface processes occurring before percolation, namely aggregation, metal oxidation, and substrate reactivity. Such findings pave the way to a rational use of O_2 as a modifier for Ag growth.

Keywords

silver, oxygen, thin film growth, sputtering deposition, surfactant effect, real time monitoring, UV-vis plasmonics, photoemission

1 Introduction

Noble metal (Ag, Au, Cu) thin films grown by physical vapour deposition on dielectrics

are involved in countless optical applications, which take advantage of their specific plasmonic and electrical properties. Common examples[1,2] include Ag-based low-emissive glazing developed by the glass industry for thermal insulation of buildings, or the use of metal films as transparent conducting electrodes (TCE) in photovoltaic devices. In all such applications, the objective of achieving metal layer continuity and smoothness at the smallest possible thickness results from a trade-off between high optical transmission in the visible range, and low electrical resistivity for infra-red light reflection or for electrical transport properties. With respect to film elaboration, the main bottleneck is the thermodynamic trend towards three-dimensional (3D) growth of noble metals on poorly-interacting dielectric substrates (such as SiO_2), driven by a poor metal/substrate adhesion and a large metal surface energy, both favouring islanding. This so-called Volmer-Weber growth follows a common sequence: (i) nucleation of clusters, most of the time on defects; (ii) growth at constant island density by adatom diffusion from the condensed gas or by direct impact; (iii) coalescence of neighbouring particles upon impingement, giving rise to more or less elongated objects depending on surface diffusion; (iv) film percolation, which leads to a conductive, though not yet continuous, metallic network; (v) filling of holes and formation of a continuous film.

Different strategies for reducing clustering and controlling this growth mechanism have been proposed, with the aim to produce thinner conductive films without compromising their optical/electrical properties. An appropriate choice of the seed layer, for instance, can alter interface energy to a certain extent by modifying interface bonding and/or favouring epitaxial growth. Since film growth is ultimately an out-of-equilibrium process, kinetics is also often used to counteract thermodynamics and to achieve more rapidly a continuous and smooth film geometry via a delayed coalescence between growing particles. By acting on diffusion lengths and nucleation density, a number of parameters such as substrate temperature or the flux and kinetic energy of impinging species can trigger earlier percolation. However, this strategy faces intrinsic limits, in terms of technical feasibility and final grain boundary density which drives to a large extend the film resistivity and its stress state. Engineering solutions based on the use of so-called buffer layers (see Ref. 3 and all references therein) or "surfactants" have been devised to obtain thinner but continuous films. These buffer layers, most of the time made of transition metals or the corresponding metal parent oxides,[4] improve the metal island wettability on the substrate by replacing relatively weak substrate/noble metal bonds with stronger metal/metal and metal/substrate bonds, increasing the sticking coefficient and changing the growth dynamics.[3] A limitation in buffer thickness is nonetheless often encountered for the final properties, in particular optical transmittance. Surfactants, on the other hand, should ideally favour a two-dimensional (2D) growth without incorporating into the film, but rather by "floating" on its surface and thus changing the surface energy of the metal. Although the term "surfactant" derived from the field of soft-matter does not necessarily describe the mechanism in an accurate way, it is often employed, as done herein, in the context of thin film growth. Based on previous surfactant studies of metal and semiconductor epitaxial growth,[5] the possibilities offered by gaseous species have been explored intensively during the recent years in the case of sputter deposition on dielectric substrates, after an earlier proof of concept for the effect of O_2 on Ag growth on amorphous silica.[6] In particular, the addition of O_2 [1,6–9] and N_2 [10,11] to the plasmagenic gas was shown to efficiently speed-up the percolation of Cu and Ag films on oxide, and even on flexible polymer substrates. Using this approach, unprecedented electrical and optical characteristics could be achieved for very thin (2.5 nm) Cu films used as TCE.[1] To avoid compromising the properties of interest through their incorporation at the growth front, low concentrations[7–9] or specific strategies for gas deployment at the initial stages of growth[9,10,12] are required. Still, a fundamental understanding of their mode of action is necessary to go beyond an empirical use.[1,7,8]

In the case of the effect of O_2 on Ag growth, which is the topic of the present work, several hypotheses have been put forward to explain an earlier film percolation. While no compound formation was detected for N_2 addition during Cu or Ag[10,11] sputter deposition, all studies based on photoemission and diffraction agree with a complex oxidation chemistry which depends on O_2 concentration in the sputtering gas and goes from the formation of Ag suboxides to a more or less crystallized and stoichiometric Ag_2O-like film.[6–9,13–16] This oxidation process requires the formation of activated oxygen species in the plasma, most likely atomic oxygen resulting from O_2 dissociation[15] as shown by the increase of plasma reactivity upon radio-frequency irradiation. By adsorbing at the surface of growing islands, oxygen could modify the surface/interface energetic balance and favor wetting in the thermodynamic sense[7] as demonstrated by the decrease of contact angle with oxygen activity in melted sessile drop measurements.[17] A similar scenario, but involving an unstable adsorbed species, was proposed for N_2.[11] But, for both gases, no direct proof has been given up to now. One of the first works put forward a role of O_2 on nucleation via a reduction of Ag diffusion at the substrate surface.[7] Other reports based on *ex situ* imaging ruled out any impact on the island density but concluded that a change in coalescence dynamics is induced by adsorbed oxygen[1,4,9,18] or nitrogen.[10] In fact, the transition from isolated islands to a percolated film is controlled by the balance between the growth rate of individual particles from the incoming atomic flux, and the rate of island coalescence *i.e.* the recovery of the equilibrium shape after impingement between two islands.[19] Thus by changing diffusion barriers, in particular at step edges (the so-called Ehrlich-Schwöbel barrier), and/or by impacting the ratio of facet orientations, oxygen can induce partial coalescence and elongated object shapes that lead to a faster apparition of an interconnected network. A similar role of oxygen produced by migration from oxygen-rich Ag[12] or ZnO[20,21] seed layers towards the growing film was also proposed. First-principle calculations assigned the "surfactant" effect to a reduction of surface energy by oxygen adsorption and to a segregation trend of O from the bulk to the surface, the so-called spillover effect.[18,21–23]

Despite previous studies pinpointing important effects such as earlier percolation and film oxidation,[1,6–9] the precise role of O_2 addition at the various stages of growth and the actual chemical state of oxidized species remain blurry. In fact, the well-know instability and reactivity of oxidized Ag compounds with the atmosphere[24–26] cast some doubts on the *ex situ* characterizations that are often used to study growth dynamics. For instance, beyond the impact of the usual protective film capping (if any) on species adsorbed at the film surface, fine chemical state analysis and quantification by depth profiling photoemission faces the question of differential sputtering and mixing artefacts. This blur overlaps with the intricate landscape of Ag 3d and O 1s core level binding energies in oxidized Ag.[24,25,27–36] This study aims at combining real-time diagnostics, namely resistivity measurements and UV-visible Surface Differential Relectivity Spectroscopy (SDRS), with *in situ* chemical analysis by X-ray Photoemission Spectroscopy (XPS) (Section 2) to unravel the role of O_2 at all Ag growth stages during magnetron sputtering deposition on SiO_2 surfaces. The question at hand, never tackled up to now, is the effect of gas composition during film growth on the interplay between chemical and morphological/structural evolutions of the film (Section 3). Besides the existence of a composition gradient in the film, different regimes of O_2 flow in the plasmagenic gas are clearly identified and discussed in the context of the O_2 "surfactant" effect and of the actual oxidation mechanism (Section 4).

2 Experimental

2.1 Film deposition

Ag films were deposited in the "MISSTIC" (Multilayer and Interfaces Sputtering deposition on STructured substrates and In situ Characterization) vacuum chamber at "Surface du Verre et Interfaces" laboratory (CNRS/Saint-Gobain Research Paris). This set-up consists of a magnetron sputtering deposition vessel (base pressure $< 2 \times 10^{-8}$ mbar) connected directly under vacuum via a load-lock to an analysis chamber (base pressure $\sim 10^{-9}$ mbar) hosting a XPS spectrometer. Ag depositions were carried out in direct current mode under Ar/O_2 mixtures, using research grade gases with a purity of 99.995 %. The constant total gas flow (50 sccm) and chamber pressure (2 μ bar) were controlled through mass flow regulators and a throttle valve in front of the turbomolecular pump. The content of O_2 in the gas flow (denoted x%O_2 hereafter) was varied between 0%O_2 and 40%O_2. One Ag deposition experiment was performed under pure O_2 (100%O_2), to provide a photoemission reference of "Ag oxide" (see below). From 0% to 40%O_2, discharge characteristics varied as follows: power 50 W; cathode voltage 396-490 V, discharge current 140-120 mA. No hysteresis was observed when increasing O_2 content. Prior to any deposition, the 2-inch Ag target (purity 99.995 %) placed at 15 cm from the substrate surface was systematically cleaned by a pre-sputtering step of 10 min. Deposition onset was controlled by a pneumatic shutter placed in front of the target. The sample was left electrically floating during growth.

Deposition rate $\mathcal{R}$ that ranged between $\mathcal{R} = 0.56$ nm.s^{-1} (0%O_2) and $\mathcal{R} = 0.48$ nm.s^{-1} (40%O_2) was systematically calibrated for each Ar/O_2 mixture by growing a ~ 50 nm thick film on a Si wafer previously marked by an ink line. The Ag film on top was etched *ex situ* in an ultrasonic ethanol bath to reveal a trench, the height of which could be measured by atomic force microscopy. By assuming a constant deposition rate over time, the nominal thickness t was defined by the product of $\mathcal{R}$ and the deposition time. Films up to $t = 20$ nm in thickness were systematically compared for all %O_2.

Si substrates (n-doped, (100)-oriented wafers purchased from Neyco, thickness 280 μm) were used as provided without specific treatment; their native SiO_2 covering layer (~ 2 nm) makes them a suitable model for silica glass while avoiding charge effects in photoemission spectroscopy. To assess the impact of an oxygen-rich plasma on the wafer surface itself during the initial deposition stages, a substrate was analysed by photoemission after an exposure during 3 s to a plasma generated on a nearby alumina target using a radio-frequency excitation (power 50 W). Due to the intrinsic very low deposition rate, the offset target position and the short exposure time, alumina signal was beyond the detection limit of XPS. At last, Ag growth under pure Ar was also monitored by SDRS on wafer treated with O_2 plasma.

2.2 Film characterization techniques

Resistivity and UV-visible spectroscopy measurements were performed simultaneously in real-time during film deposition to get some insights on the thickness thresholds for different stages of film growth: island growth, particle coalescence, percolation and continuous film formation. The chemistry and composition of the deposited films were characterized at a given thickness by *in situ* photoemission. *In situ* conditions are ideal for such a surface-sensitive method, since they avoid exposure to the atmosphere and oxide ageing, thus eliminating the need for protective capping layers and changes in chemical states induced by sputtering during *ex situ* XPS depth profiling. For instance, alongside an evolution of film stoichiometry, the formation of Ag_2CO_3 compound combined with hydroxylation has previously been reported upon interaction of Ag oxide with atmospheric CO_2 and H_2O.[6,24–26,32,37,38] Films were also characterized *ex situ* by Transmission Electron Microscopy (TEM) and X-Ray Diffraction (XRD).

In situ XPS was performed with a Phoi-

bos 100 hemispherical analyser (from SPECS) equipped with 5 channeltron detectors under non-monochromatic Al Kα excitation (XR50 from SPECS). Binding energy (BE) scale was calibrated on the Ag 3d 5/2 core level of a thick metallic Ag film ($E_B = 368.1$ eV). Spectra were recorded at a pass energy of 15 eV and for an emission angle of 24.5 deg. The acquired Ag 3d, O 1s, C 1s, Si 2p core level regions were analysed with the *I4P Igor Pro* package.[39] Besides an active background (Shirley type for O 1s and Tougaard type for Ag 3d) and the account of source satellites, all peaks were decomposed using (i) a Voigt profile or (ii) a Doniach-Sunjic asymmetric line shape (asymmetry parameter of 0.05) convoluted with a Gaussian in the case of metallic Ag (see 39 and references therein). The Lorentzian full-width at half maximum (FWHM) of peaks was fixed at the Al-Kα_1 source emission line (0.58 eV)while the Gaussian FWHM counterpart of the profile was assigned to instrumental broadening and distribution of chemical shifts. The branching ratio and the spin-orbit splitting of Ag 3d doublet was kept fixed at the theoretical (2/3) and the tabulated (6 eV[40]) values, respectively. For spectra involving a large fraction of metallic Ag, a bulk plasmon loss shifted by about 3.85 eV had to be taken into account in Ag 3d profile as well as similar feature but shifted by 12 eV for oxidized silver. Quantification of species[39] was performed after correcting the corresponding core level peak areas from photo-ionization cross section and analyzer transmission function[41] using TPP2M inelastic mean free path in metallic silver ($\lambda^{Ag}_{Ag3d} = 1.6$ nm. $\lambda^{Ag}_{O1s} = 1.43$ nm). Beyond model bias, the error bars are of ± 0.1 eV for BE and of ~ 10 % for area quantification. Despite the *in situ* transfer, a slight carbon contamination of a fraction of Ag(111) monolayer ($\sim$ 0.3) was present at the surface of all samples. Its presence does not entail the following discussion as its BE corresponds to hydrocarbons ($E_B = 284.5$ eV) and not C-O bonds ($E_B = 286 - 288$ eV[40]) or even Ag carbonates ($E_B = 287.6 - 288$ eV[24,25,28,32,42]). No other contaminants, particularly implanted Ar, were detected.

Real-time film resistivity measurements were carried out with a set-up with two electrodes.[43] 200 nm-thick linear electrodes (size 31×2 mm^2; see inset of Figure 1) separated by 25 mm were used to inject the current and measure the voltage drop; the corresponding measured sheet-resistance values $R^m_\square$ were recorded at a rate of 10 Hz with a custom-made set-up (Alciom company). The $R^m_\square$ value was further corrected using a previous calibration against an *ex situ* 4-point measurement[43] (RT-3000/RG-80N system from Napson) to obtain the corrected sheet-resistance value ($R_\square$). Film resistivity $\rho(t)$ was obtained by multiplying $R_\square$ by the nominal film thickness $\rho(t) = R_\square(t) \times t$.[43] The maximum of the product $\rho(t) \times t = R_\square(t) \times t^2$ versus t[44] was then used to locate the percolation threshold t_p that corresponds to the appearance of a continuous electrical path between electrodes.

Growth was also followed by UV-visible SDRS. The set-up is described in depth in Refs. 19,45,46. In brief, a UV-visible beam (wavelength 275-820 nm or photon energy 1.5-4.5 eV) emitted by a deuterium-halogen lamp was focused on the sample through transparent fused silica viewports at an incidence angle of 45°. The reflected beam was then split by a $BaBO_3$ Wollaston prism in its s (perpendicular to the incident plane) and p (parallel, respectively) polarization states. The two beams were then collected and analysed separately by two grating broadband UV-Vis spectrometers (from Avantes) to record the relative variation of the sample reflectivity $\frac{\Delta R}{R}$ with respect to the signal recorded on the bare substrate prior to deposition. Spectra were corrected from source drift through an ancillary spectrometer. Most of the beam paths were inside solarized fibers. The acquisition rate was about 15 spectra.s^{-1} consisting of an average of 25 measures with an integration time of 2.5 ms. As was previously shown,[45,47] this SDRS signal is mainly driven by the excitations of plasmon resonances in the growing nanoparticles. To obtain information on their morphology from their optical response, in particular on their aspect ratio

(diameter/height) and oxidation state, experiments were supplemented by dielectric simulations with regular arrays of truncated sphere shapes using the *GranFilm* software.[48] Reflection coefficients are calculated in the framework of the excess fields and surface susceptibilities of Bedeaux and Vlieger.[49] These quantities depend mainly on the tensor of polarizability of the nanoparticles, which is calculated in the quasi-static approximation by solving the Laplace equation. Particles arranged on a square lattice are electrostatically coupled at quadrupolar order. Oxidation is described by a core-shell geometry.[50] To account for experimental widths due to finite-size effects and size/shape distributions, an *ad hoc* broadening[50] was included to simulate experimental widths via a convolution with a Gaussian function (with a FWHM of 0.4 eV and 0.1 eV for the parallel and perpendicular directions, respectively). Bulk dielectric functions of Ag, SiO_2, Ag_2O[51,52] were used for the simulations. A detailed description of the underlying optical models can be found in Refs. 45,47,49,50,53–55. Besides trends obtained by comparing experiments and simulations, the integrated normalized intensity of s-polarized spectra is also informative:

$$\mathcal{A}_s(t) \propto \frac{1}{t}\int \frac{\Delta R_s}{R_s}(\omega,t)\frac{d\omega}{\omega}. \qquad (1)$$

This quantity is, in fact, proportional to the oscillator strength of the parallel plasmon excitation, and thereby can also be used as a direct reporter of the evolution of particle aspect ratio.[47]

In order to determine the impact of $\%O_2$ on deposited particle density and size, samples at an equivalent nominal thickness of 0.6 nm were analysed by TEM plane view. The Scanning Transmission Electron Microscope High Angle Annular Dark Field (STEM-HAADF) acquisitions in plane-view mode were performed on the Titan THEMIS (ThermoFischer, Equipex TEMPOS) of the PANAM platform (C2N, Palaiseau, France). It features a 200 keV high-brilliance XFEG gun with a Cs corrector on the condenser system allowing 80 pm of lateral resolution. The selected thickness ensures that all films, regardless of their deposition conditions, are well below t_p and consist of disconnected nanoparticles. Films were deposited on 15 nm thick silicon nitride membranes (with nine separated windows of 100×100 μm^2, Pelco from Ted Pella inc.), whose oxidized surface mimics the SiO_2 native oxide layer of the Si wafer. Right after Ag film deposition, all samples were capped with a 5 nm thick aluminium-doped ZnO protective layer deposited from a ceramic target under pure Ar. Samples were synthesized just before TEM analysis and stored under vacuum or controlled atmosphere to minimize ageing. TEM images were analysed with a *Python* image analysis script coupling a "blob" algorithm to distinguish Ag nanoparticles from membrane surface capped by AZO, and a watershed procedure for finding their edge and thus their in-plane shape.

20 nm thick films deposited at different $\%O_2$ conditions were analysed by XRD (i) in the $\theta-2\theta$ Bragg-Brentano geometry (Bruker D8 Advance apparatus) and (ii) at grazing incidence (Rigaku SmartLab; incidence 0.5 deg) with a copper Kα source combined with a monochromator. Samples were deposited on bulk amorphous SiO_2 wafers (from Neyco, thickness 1 mm) to avoid the overlap between the peaks of interest and the multiple diffraction Si(100) signal in the $2\theta = 30-35°$ range.[56] The same capping and manipulation caution as for the TEM samples was employed. Diffractograms were compared to expectations from bulk atomic structures: (i) face centred cubic Ag, $Fm\bar{3}m$, a_B = 4.09 Å, (ii) cuprite Ag_2O, $Pn\bar{3}m$, a_B = 4.72 Å, and (iii) wurtzite ZnO, $P6_3mc$, a_B = 3.25 Å, c_B = 5.21 Å.

3 Results

3.1 Resisitivity measurements

As previous reports have pointed out,[4,6–8,14,20] the addition of O_2 has a drastic impact on

the evolution of film resistance with nominal thickness as seen in Figure 1-a. The large initial resistance corresponds to electrical transport through the silicon wafer in the growth stage of disconnected islands. A sharp decrease is observed at t_p when an electrical path is established by the film between the two electrodes. Better determined as the maximum in the $\rho(t) \times t$ curve (Figure 1-b), this onset (Figure 2) shifts downwards in thickness with $\%O_2$, much more rapidly from 0% to 4% than later on. In parallel, resistivity values at $t = 20$ nm (Figure 2) show an over tenfold increase between $0\%O_2$ and $40\%O_2$. Both characteristics point to a an important change of the film microstructure and chemistry induced by the introduction of O_2 in the plasmagenic gas.

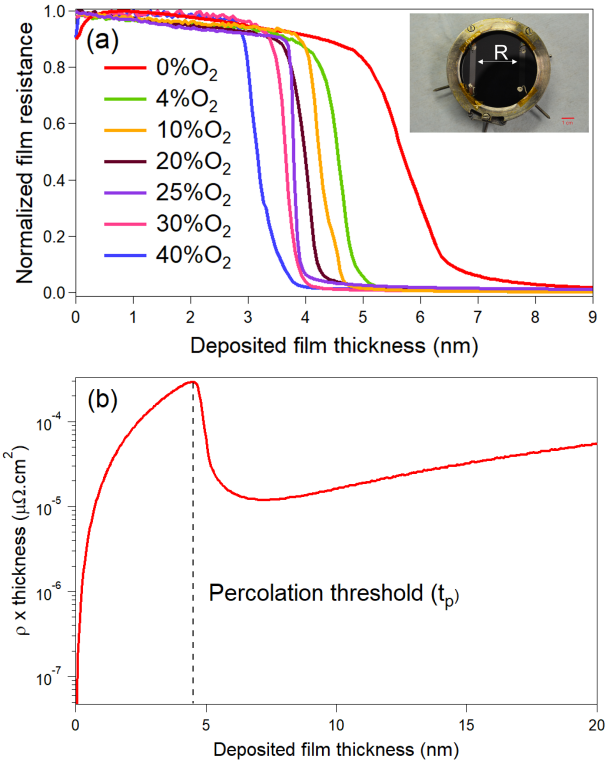

Figure 1: (a) Real-time film resistance during Ag film deposition on SiO_2/Si wafer as a function of $\%O_2$ in the gas flow. Data are normalized to the value prior to shutter opening. The inset shows a picture of the electrodes at the surface of the substrate. (b) Example of $\rho(t) \times t$ evolution for a deposition under $4\%O_2$. The sharp decrease in resistance in Figure a and the maximum in Figure b correspond to the formation of a percolated film.

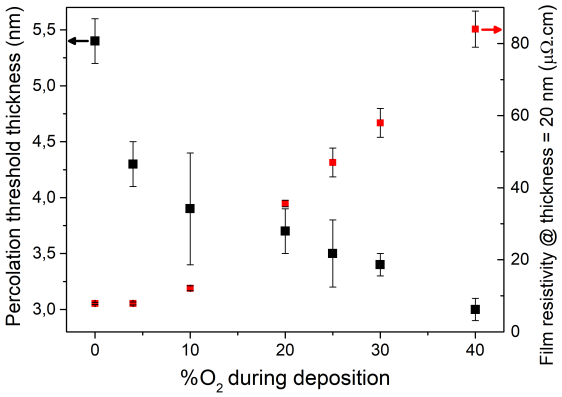

Figure 2: Percolation thickness threshold t_p for films deposited under different $\%O_2$ and film resistivity at the final thickness of $t = 20$ nm. In both cases, values and error bars result from an average over different experiments.

3.2 *In situ* XPS measurements

The impact on Ag film chemistry, namely its oxidation state, was first explored by recording O 1s and Ag 3d core levels (Figure 3) at a thickness of $t = 20$ nm, which is enough for the substrate signal to be completely damped by the overlayer ($3\lambda \sim 5$ nm in Ag). In parallel to the increase of a new O 1s feature at $E_B \sim 529.2$ eV, the BE value for the Ag 3d 5/2 peak shifts continuously from $E_B = 368.1$ eV down to $E_B = 367.7$ eV when going from pure Ar ($0\%O_2$) to pure O_2 ($100\%O_2$). This negative chemical shift observed upon Ag oxidation, although counter-intuitive in the sense of the initial state electrostatic picture, results from the lack of on-site sensitivity to oxidation in Ag and complex final state effect.[27,57] Both extreme BE are in close agreement with reported values for Ag^0 and Ag^+ oxidation states in metallic Ag [$E_B(Ag\,3d) = 368.1 \pm 0.15$ eV] and Ag_2O [$E_B(Ag\,3d) = 367.7 \pm 0.3$ eV; $E_B(O\,1s) = 529.2 \pm 0.35$ eV][24,25,27–35] [1]. Although debated,[35] the spectroscopic fingerprints of AgO found at $E_B(Ag\,3d) = 367.5 \pm 0.4$ eV and $E_B(O\,1s) = 528.5 \pm 0.4$ do not match with the present findings under pure O_2. In fact,

[1] The reported values and standard deviations of binding energies result from an average over the quoted literature on oxidized Ag.

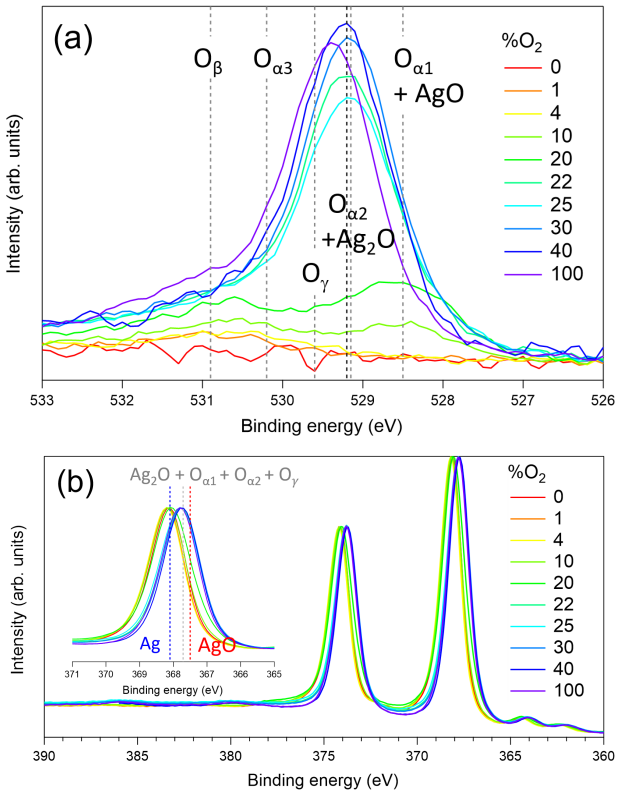

Figure 3: Evolution of core level regions of a 20 nm thick Ag films deposited under increasing %O_2: (a) O 1s and (b) Ag 3d. Spectra are normalized to background in Figure a and to same scale in Figure b. The inset in Figure b shows a zoom of the Ag 3d 5/2 component. The evolution of O 1s feature and the shift of Ag 3d BE prove the progressive oxidation of Ag. Vertical dotted lines correspond to tabulated values (see text).

AgO and Ag_2O compounds differ in terms of atomic structures.[35] The cubic cuprite Ag_2O, which is the most stable Ag oxide polymorph, involves O anions in a four-fold Ag^+ tetrahedral coordination. The monoclinic AgO is a mixed valence compound with an average oxidation state of +2 but involving a dismutation on the two Ag sites, with Ag^+ in a linear coordination and Ag^{3+} in square-planar configuration. The +3 unstable higher oxidation state has been reported only in exotic compounds such as Ag_2O_3, but their syntheses require harsh oxidizing environment such as anodic treatment or ozone exposure.[24,25,33,58] The hierarchy of thermodynamic stability Ag > Ag_2O >AgO > Ag_2O_3 even predicts, in principle, the instability of all Ag oxides in vacuum at room temperature.[26,35,58] The spectroscopic landscape in photoemission for bulk compounds (Ag_2O and AgO) is blurred by the formation of carbonates at their surface upon exposure to air and their poor thermal stability[24,25,27–29,32,37] that prevent any faithful in-vacuum preparation procedure. Spectroscopic distinction between Ag^+ and Ag^{3+} in AgO is not even clear-cut in the literature, with many reports describing a broad Ag 3d peak that accounts for the two crystallographic sites. Regarding direct photoemission from *in situ* oxidized Ag that escapes the inherent problem of contamination,[30,34–36] the spectroscopist faces the presence of suboxides, whose atomic structures are almost never determined. Besides defined bulk compounds, several oxygen moieties with distinct stability in temperature have been reported during oxidation of metallic Ag single crystal surfaces with molecular O_2 at high temperature.[30,36,37,59–64] Upon heating, physisorbed O_2 partly dissociates leaving an atomic species (labeled $O_{\alpha1}$) that desorbs above 580 K. This species observed at low chemical potential in many surface science experiments is associated to orientation-dependent surface reconstructions. Increasing the O_2 exposure and/or temperature leads to the migration of oxygen into the bulk (labelled O_β) and the creation of a partial equilibrium with the surface species. This O_β subsurface species polarizes the surface Ag-O bond, creating different moieties

from a spectroscopic point of view *i.e.* $O_{\alpha 3}$. Their presence seems to be correlated to the density of defects.[36] At an even higher chemical potential, in particular near-atmospheric pressure and high-temperature, the Ag surface strongly restructures leading to a strongly bound and thermally stable subsurface O_γ oxygen species in conjunction with a $O_{\alpha 2}$ moiety at its surface. This Ag oxidation pathway requiring high-pressure dosing due to the very low-sticking coefficient of O_2[15,59] can be sped-up by exposing the Ag surface to atomic oxygen produced by a dedicated source[31,33,63] or in the course of reactive sputtering deposition[15] as done herein. To sum up, upon increasing oxygen chemical potential, the formation of O moieties follows the schematic pathway:

$$\begin{aligned} O_{\alpha_1}(s) &\rightarrow O_\beta(b) + O_{\alpha_3}(s) \rightarrow O_\gamma(b) + O_{\alpha_2}(s) \\ &\rightarrow O_{Ag_2O}(b) \rightarrow O_{AgO}(b) \end{aligned} \quad (2)$$

where the labels $(s), (b)$ stand for "surface" and "bulk or subsurface", respectively. Besides the use of their different desorption temperatures, these O species are often identified via their O 1s photoemission fingerprints. Often overlapped, they are reported at[30,36,37,59–64] (see dotted lines in Figure 3-a): $E_B(O_{\alpha 1}\,1s) = 528.1-528.4$ eV, $E_B(O_\beta\,1s) = 530.8-531.0$ eV, $E_B(O_{\alpha 3}\,1s) = 530.1-530.4$ eV, $E_B(O_\gamma\,1s) = 529.5-529.7$ eV, $E_B(O_{\alpha 2}\,1s) = 529.1-529.2$ eV.

A close inspection of the O 1s core level spectra shown in Figure 3-a reveals the presence of several evolving components. As shown in the examples of Figure S1-a,b of supporting information for 20 nm thick films grown under different $\%O_2$ conditions, a consistent fit could be systematically achieved for all O 1s spectra using a sum of Voigt peaks corresponding to all the species reported in the literature. But, owing to the poor resolution of the non-monochromated source and the large number of fit parameters, their binding energies were kept fixed at values discussed above while a common Gaussian FWHM was used. Figure 4-a shows the evolution of the relative area of all components used in the fit of the O 1s core level a function of $\%O_2$ at $t = 20$ nm. On the other hand, the reported chemical shift of Ag 3d upon oxidation,[64] than spans from -0.35 to -0.6 eV, is less sensitive to the formed species or bulk compounds (Figure 3-b, inset). Therefore, the fit of Ag 3d core level was performed only with two components, as exemplified in Figure S1-c, with one component for metallic Ag at fixed $E_B(Ag^0) = 368.1$ eV, and a second generic component for oxidized silver, that was found shifted by -0.5 ± 0.1 eV. Assuming a global $Ag^0_{1-y}Ag^{\delta+}_y$ composition, the fraction y of oxidized silver could be then obtained from the ratio of peak areas in the Ag 3d decomposition. In addition, from the area ratio O 1s/Ag 3d, a global average stoichiometry AgO_x could be deduced assuming a uniform film and using inelastic mean free paths in metallic silver. Both results could then be combined to deduce the average charge δ transferred per Ag atom using the balance $2x = \delta.y$. All quantities are displayed in Figure 4-b for 20 nm-thick films.

Below $10\%O_2$ (Figure 4-a), oxidation proceeds via a mixture of O_{α_1}, O_β and O_{α_3} moieties, in which the main species O_β and O_{α_3} evolve in parallel as expected (see Equation 2). These O 1s contributions cannot be entailed by a Ag_2CO_3-like carbonate species which is close in BE ($E_B = 530.5 \pm 0.3$[24,25,28,29]) since the observed C 1s BE ($E_B = 284.5$ eV; Figure S2) does not correspond to carbonates ($E_B = 287.6 - 288$ eV[24,25,28,32,42]). Any contribution from hydroxyl groups or adsorbed water can also be safely ruled out, as they peak at $E_B > 531.5$ eV[32,42] and are not observed in the present data. At last, the lowest O 1s BE component at $E_B = 528.1 - 528.4$ eV (O_{α_1}) cannot be ascribed to AgO, since its formation before that of Ag_2O is thermodynamically unlikely, and the corresponding Ag 3d chemical shift is not observed (inset of Figure 3-b). The interpretation is further reinforced by the quantification of the total (O_{α_1}+O_{α_3}) O 1s signal. Considering it as coming from only surface species, the total coverage is always found well below the Ag(111) monolayer (< 0.8); on the other hand including O 1s signal at $E_B = 529.1 - 529.2$ eV (*i.e.* interpreting the signal as O_{α_2} instead of Ag_2O) leads to unphys-

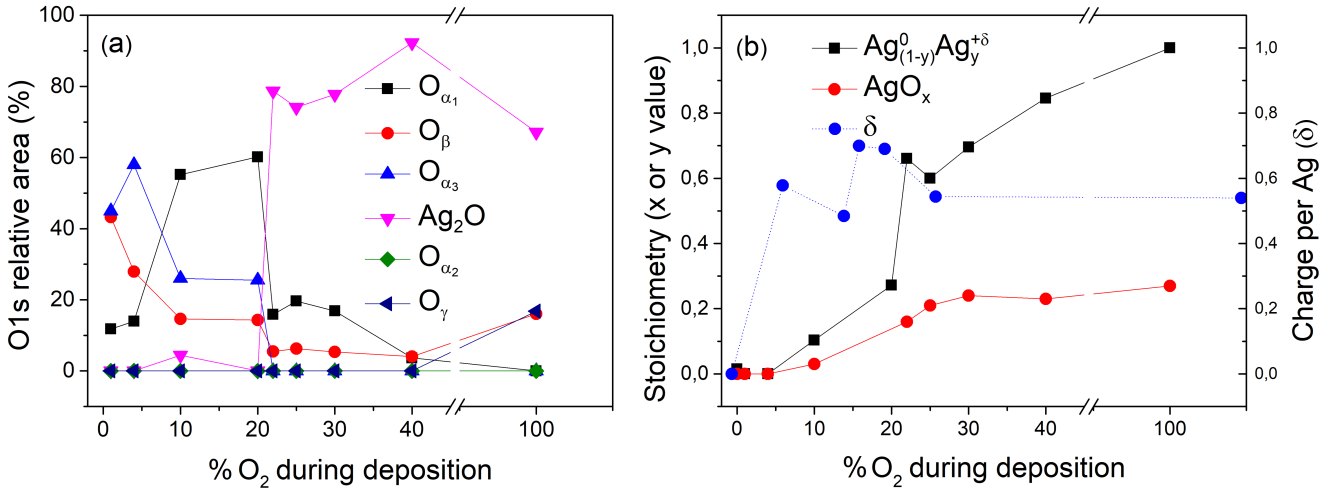

Figure 4: Photoemission analysis of 20 nm-thick films as a function of $\%O_2$: (a) evolution of the relative area of all O 1s components (see text for explanations) and (b) changes in (i) global stoichiometry AgO_x from O 1s/Ag 3d relative peak areas (red symbols), (ii) fraction $Ag^0_{1-y}Ag^{\delta+}_y$ of oxidized Ag component from the Ag 3d core level spectra fits (black symbols) and (iii) the charge transferred δ per Ag atom (blue symbols). The error bars are of the order of 10 %. An uniform film hypothesis is used for the analysis.

ical coverage well above the monolayer. At last, to obtain some insight on the oxidation process, a film of a 15 nm-thick Ag film deposited under pure Ar was exposed to $10\%O_2$ but without plasma (Figure S3). Since only O_β and O_{α_3} species are observed in its O 1s spectrum, it seems that below 10 $\%O_2$, the oxidation of Ag is driven by the interaction with molecular oxygen leading to the absence of significant Ag 3d chemical shift as already reported for O_{α_3}-O_β.[36] The increase from 10% to $20\%O_2$ leads to the replacement of O_β and O_{α_3} moieties by O_{α_1} and to a more sizeable fraction of oxidized Ag associated to a higher value of δ (Figure 4). Such a higher oxidic nature of $O_{\alpha 1}$ has already been pointed out in Ref. 36 which reports a $Ag^{\delta+}/O$ value as more than 20 times higher than for O_{α_3}-O_β. The sharp transition observed at $20\%O_2$ (Figure 4) corresponds to the appearance of an O 1s component at $E_B = 529.2$ eV and a noticeable change in stoichiometry and fraction of oxidized Ag. The new O 1s peak is assigned to the formation of an Ag_2O-like compound, and not to the O_{α_2} moiety, since its companion O_γ peak is never observed (see Equation 2). Interestingly, not present at lower $\%O_2$, a not clearly assigned spin-orbit split "plasmon-like" feature at $E_B = 379.6$ eV, shifted by +12.3 eV from metallic Ag 3d, goes with the appearance of this Ag_2O-like compound. In contrast, the plasmon loss in metallic Ag, shifted by +3.85 eV, has to be accounted for only below ~ 20 $\%O_2$.

Even for deposition under pure O_2, the global stoichiometry AgO_x, including all O species, remains surprisingly well below the $x = 0.5$ value expected for Ag_2O, while the charge transferred per Ag atom does not reach the expected value of 1 (about 0.6) (Figure 4). The riddle about the formation of suboxides is solved when looking at the uniformity of composition along the film thickness at three representative oxygen flow conditions: $4\%O_2$, $10\%O_2$ and $40\%O_2$ (Figure S4-Figure 5). Thickness values were chosen in order to span the different stages of Ag film growth: (i) disconnected Ag islands growth on the surface, (ii) near the percolation threshold thickness, and (iii) a final thickness above percolation (see Figure 2). The evolution of chemical states with increasing film thickness was analysed by fitting core levels similarly to the 20 nm-thick films. Nevertheless, for thickness values below about $3\lambda \sim 5$ nm, an extra

O 1s component at $E_B = 532$ eV corresponding to SiO_2 from the substrate surface had to be accounted for due to its partial damping and/or to the metal film discontinuity (Figure S4 and S5). Results for the evolution of different O 1s components with increasing thickness are gathered in Figure 6 and those for the fraction $x-y$ of oxidized Ag, stemming from Ag 3d spectra analysis in Figure 5 for the three aforementioned $\%O_2$.

At $4\%O_2$, no lineshape evolution of the Ag 3d spectrum with thickness is observed. Conversely, as seen the change of stoichiometry with thickness at 10% and $40\%O_2$ (Figure 5), as soon as Ag_2O-like fingerprints are detected in photoemission, a gradient in Ag oxidation state sets up during deposition starting with a more metallic film at the interface with the substrate before reaching a steady state at larger thickness. Noteworthy, modulo the XPS probing depth, the transition starts at the film percolation (see Figures 5-6) and the plateau is reached when a continuous film is formed. Previous works reported on the concomitant formation of Ag suboxides and of metal.[7–9,13–16,18,26] Only recently,[23,65] a depth-dependent profile of oxidation was evidenced indicating a higher O concentration near the film surface. It was assigned via first-principle calculations to an out-diffusion of O to the surface during growth, the so-called oxygen spillover.[18,21–23] As seen in the present measurements Figures 5-6, the composition gradient and the nature of O species appear to be correlated to the morphology and the film percolation. In parallel to the previously proposed mechanism of O-spillover, a likely explanation involves a competition between favourable Ag clustering at the SiO_2 surface due to fast ad-atom diffusion, and Ag oxidation by direct impinging of activated O species from the plasma[15] via an "Eley-Rideal" mechanism. Indeed, a "Langmuir-Hinshelwood" scenario involving oxygen surface diffusion is impeded by the competition with the substrate oxidation. This latter is evidenced by photoemission analysis of the Si wafer before and after Ar-O_2 plasma exposure in front of an alumina target (see Section 2). For the explored exposure (3 s corresponding to ~ 1.5 nm during deposition), the plasma treatment is accompanied by (i) a nearly complete reaction of activated O species with carbonaceous contamination surface species as compared to pure Ar (Figure 7-a), and (ii) a SiO_2 thickening of about 0.2 nm (ratio Si^{4+}/Si^0 2p), alongside a sizeable Si upward band bending of 0.4 eV (Figure 7-b). Thus, due to this competing mechanism, as soon as the formation of bulk suboxides ($\%O_2 \geq 10$), the oxidation rate of Ag should increase with surface coverage, and reach a stationary value above film percolation.
At last, the exposure to molecular O_2 of a metallic Ag island deposit (1.5 nm) gives rise only to a modest uptake of O_β and O_{α_3} species and no band bending in the wafer (Figure 8). At the opposite, when activated species are present in the plasma even at low $\%O_2$, substrate and Ag particles actually oxidize as demonstrated by the increase of the Ag_2O photoemission fingerprints (Figure S6) and the more sizeable shift of the Si 2p core level than after exposure to a pure Ar plasma (Figure 8). After an exposure of 90 s to the plasma, the rise-up of stoichiometry to a value closer to Ag_2O ($x = 0.1$ at $4\%O_2$ and $x = 0.42$ at $20\%O_2$) and much larger than during growth (Figure 5) even under $100\%O_2$ ($x = 0.28$) demonstrates that the Ag oxidation phenomenon promoted by activated O species in the plasma is not really impeded. This point is confirmed by SDRS (Figure S7); while metallic nanoparticles seem insensitive to exposure to an Ar plasma, their plasmonic response clearly fades away with oxidation under the plasma. Thus even if thermodynamic trend of segregation of O to the surface is predicted by *ab initio* simulations,[18,21–23] kinetics is also involved in the presence of metal during growth.

3.3 *Ex situ* x-ray diffraction

Photoemission results have been supplemented by *ex situ* out-of-plane Bragg-Brentano and in-plane grazing incidence XRD (Figure 9). Compared to bulk atomic structure expectations, all diffractograms exhibit only Ag and

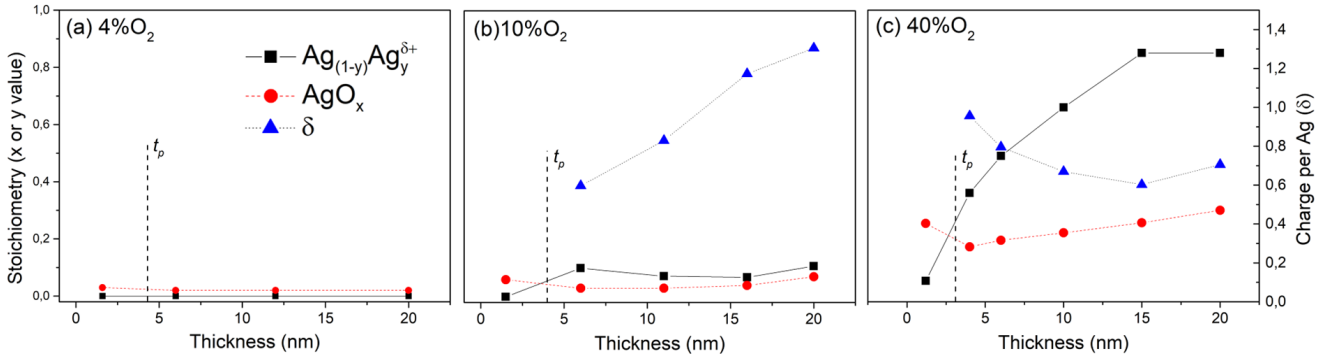

Figure 5: Same as Figure 4-b but increasing thickness for (a) 4%O_2, (b) 10%O_2 and (b) 40%O_2 during deposition.

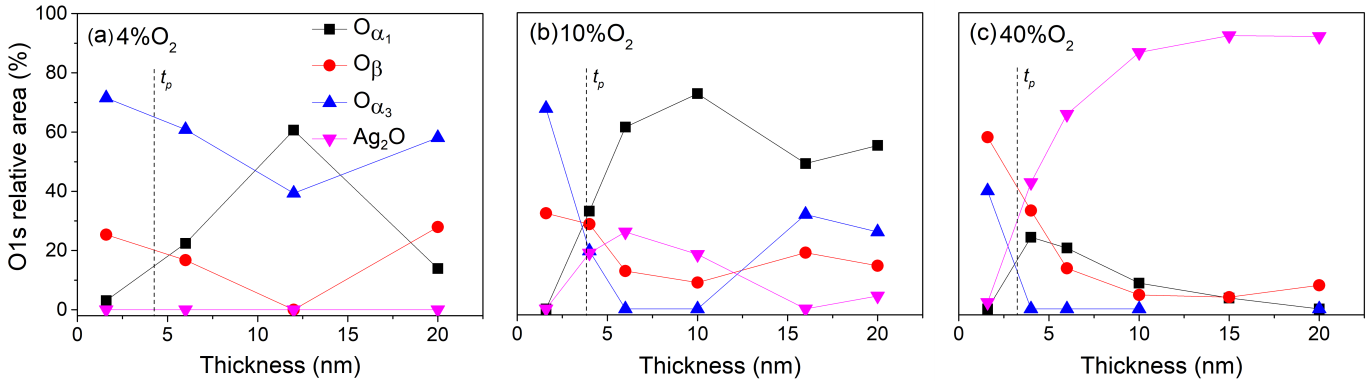

Figure 6: Evolution of the relative area of all O 1s components (see text for explanations) as a function of film thickness, for depositions at (a) 4%O_2, (b) 10%O_2, and (c) 40%O_2. The vertical dotted line corresponds to percolation threshold. The error bars are of the order of 10 % of the value.

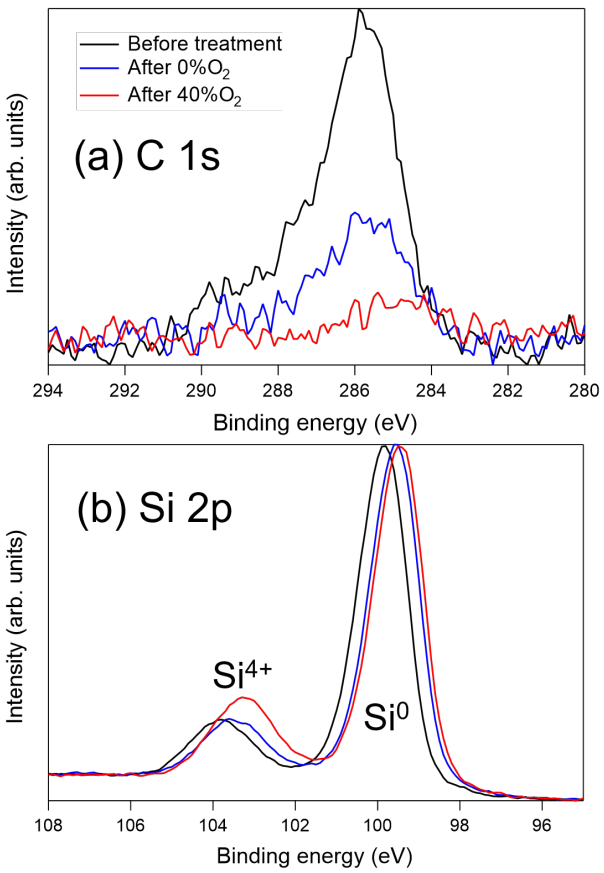

Figure 7: Evolution of core levels after a plasma treatment of the Si wafer surface in a pure Ar plasma ($0\%O_2$) and a $40\%O_2$ mixture: (a) C 1s and (b) Si 2p. The time scale of plasma treatment (3 s) is equivalent to a deposited thickness of $t \sim 1.5$ nm.

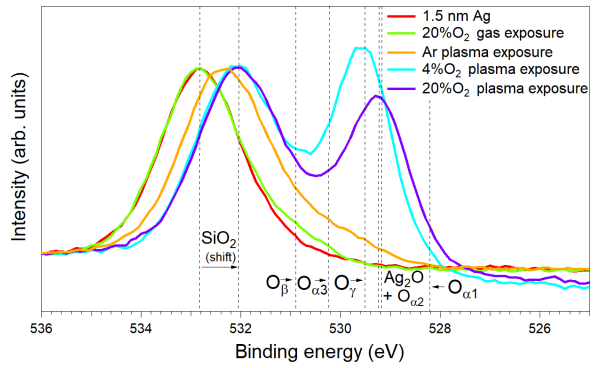

Figure 8: Evolution of O 1s core level of a 1.5 nm thick Ag film deposited under pure Ar (red line) induced by an 90 s exposure (i) to molecular O_2 (green line) and (ii) to a plasma generated on a nearby alumina target with $4\%O_2$ (violet line) and $20\%O_2$ (blue line). The dotted vertical lines correspond to the BE values of the different expected O species.

ZnO peaks with a broad feature associated to amorphous SiO_2. The most intense (111) reflection of Ag_2O, expected at $2\theta \simeq 33°$, is absent in all diffraction geometries and for all $\%O_2$. The fortuitous overlap between $(111)_{Ag}$ and $(200)_{Ag_2O}$ reflections cannot hide textured Ag_2O grains, since the expected $(220)_{Ag_2O}$ peak along the perpendicular diffraction direction is not observed. Thus, the formed silver oxide does not appear to be crystalline, in agreement with similar studies of sputtering deposition[14,20] although other studies have observed crystallized sputtered Ag_2O films.[6–8,13,16] Different film thicknesses, deposition kinetics and substrates may explain the discrepancy. Peak positions, FWHMs and areas extracted from a global fit with Voigt line shapes have been translated into strain ϵ, coherent domain size D_{coh} and volume ratio (Figure S8 and inset of Figure 9). The [001]-textured ZnO layer has a perpendicular D_{coh} close to its film thickness and shows an anisotropic distortion due to an in-plane compression stress. In comparison, the [111]-oriented Ag grains appear to be poorly strained, unlike the [100]-oriented grains which are in a tensile strain along both directions (Figure S8-a). D_{coh} obtained from all Ag peaks decreases with $\%O_2$, the most impacted peak being the out-of-plane $(111)_{Ag}$, demonstrating a clear loss of crystallinity of metallic Ag (Figure S8-b). Surprisingly, a switch of out-of-plane texture from [111] to [100][14] (inset of Figure 9) parallels the change in oxidation behaviour observed by XPS at $10\%O_2$ (Figure 4).

3.4 Real-time surface differential reflectivity spectroscopy

To understand the impact of the film chemical evolution on morphology, Ag growth was probed in real-time by SDRS in parallel to resistivity measurements. Figure 10 shows the comparison between *p*-polarized spectra for different $\%O_2$, at given thicknesses of 0.6 nm and 3 nm, corresponding to isolated nanoparticles far from and just before percolation, respectively (Figure 2). Signal line shape stems from the characteristic excitations of the parallel and

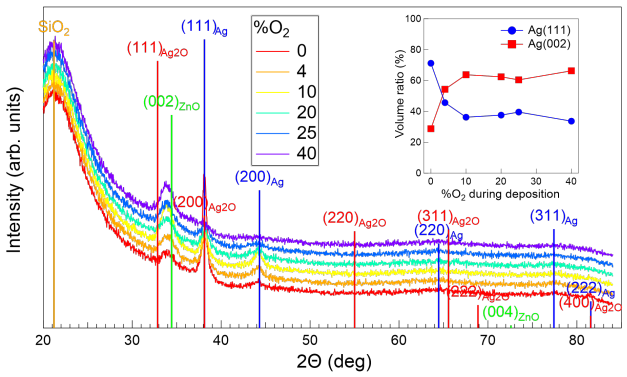

Figure 9: Bragg-Brentano XRD measurements of 20 nm-thick films deposited on SiO_2 substrates under different $\%O_2$ conditions. Vertical bars correspond to expected diffraction peak positions and relative intensities for bulk compounds: Ag (blue), Ag_2O (red), ZnO (green) and SiO_2 (orange). The inset shows the corresponding analysis of texture as a volume ratio given by the fraction of $(111)_{Ag}$ and $(200)_{Ag}$ out-of-plane peak areas corrected from expected bulk powder intensities.

perpendicular plasmon resonances in the growing Ag nanoparticles; they manifest in the form of a broad positive peak at low energy (2-2.5 eV) for the former, and a sharper negative feature at higher energy ($\sim$ 3.8 eV), for the latter.

Without going up to a quantitative fit of SDRS spectra,[19,55] dielectric simulations (Figure 11) with the *GranFilm* package were performed in *p*-polarization for Ag truncated spheres on a semi-infinite SiO_2 substrate, in order to pinpoint the main effects on the optical response of (i) Ag nanoparticle aspect ratio A_r (diameter/height) (Figure 11-a), (ii) Ag nanoparticle density ρ_s (Figure 11-b) and (iii) the formation of an "Ag_2O" shell of thickness t_s (Figure 11-c). In the first two cases, sphere truncation and lattice spacing were sequentially varied, while in the last case relative shell thickness was continuously increased to mimic an oxidation process. While the calculated electrostatic interaction was taken with SiO_2, all differential reflectivity spectra have been normalized to the reflectivity of Si, to compare simulated and experimental $\frac{\Delta R}{R}$ values. Simulations were performed at constant deposited thickness, to highlight variations related to os-

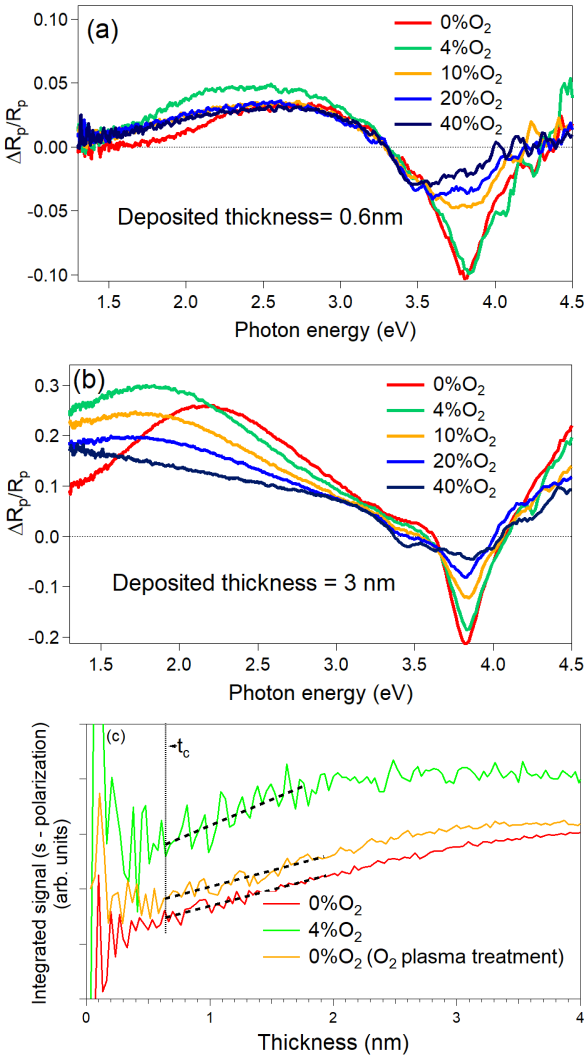

Figure 10: Evolution of the p-polarized SDRS spectra for different $\%O_2$ during deposition at a nominal deposited film thickness of (a) 0.6 nm and (b) 3 nm. (c) Integrated value $\mathcal{A}_s(t)$ (Equation 1) of the s-polarized SDRS spectra for $0\%O_2$ [without (red line) and with $40\%O_2$ wafer plasma pre-treatment (orange line)] and $4\%O_2$ on a native wafer. Trends similar to 4 $\%O_2$ are found at higher oxygen flow (not shown for clarity). The vertical dotted line points to the early coalescence t_c.

cillator strength.[45,47] Indeed, one should keep in mind that the total SDRS signal scales linearly with film thickness.[47]

In brief, as can be seen in Figure 11-a, and as previously described,[45,47,53–55,66] particle flattening (Figure 11-a) induces sizeable red shift and intensity increase of the low-energy parallel plasmon resonance. The effects on the the high-energy perpendicular plasmon resonance are quite the opposite but much less pronounced. Similar trends are observed with the increase of particle density (Figure 11-b), but with a more moderate effect on the low-energy resonance.[66] Lastly, thickening the oxide shell red-shifts the position of both resonances and decreases their intensities[50] (Figure 11-c); this latter effect is basically related to a lower fraction of polarizable metallic Ag in the nanoparticles. Overall, the low energy resonance peak is a better indicator of morphology change than the high energy one, due to the presence of interband transitions in the dielectric function of Ag. A combination of these three effects, changes in aspect ratio, density and oxide shell formation, contributes in measurements of Figure 10 and will be discussed in the next sections.

To assess the above described impact of substrate interaction with reactive oxygen species, the Ag growth under pure Ar on a native oxide-covered substrate was compared to that on a wafer pre-treated by exposure to a 40%O_2 plasma for 3 s (Figure S9). While no difference on percolation threshold t_p was observed (not shown), optics does not evidence a significant change in aspect ratio although a variation of density remains possible.

As a support, to highlight the evolution of A_r,[47] SDRS signal in s-polarization was also integrated according to Equation 1 (Figure 10-c) up to late coalescence where $\mathcal{A}_s(t)$ saturates because of the limited spectral integration range of the plasmon peak (> 1.5 eV). Deposition under pure Ar (0%O_2) on as-introduced and plasma-treated wafers is compared to 4%O_2. Even if the initial U-shape evolution of $\mathcal{A}_s(t)$ observed systematically for vapour deposition of metals on dielectrics[47] is blurred by the

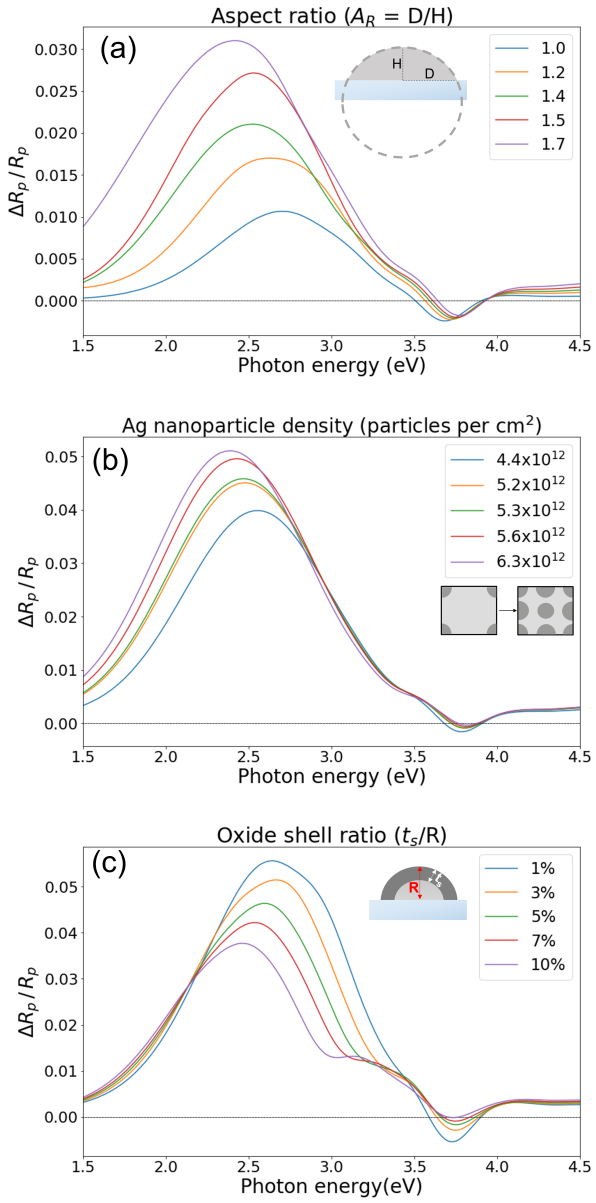

Figure 11: Simulated SDRS spectra for Ag truncated spheres arranged in a square lattice on SiO_2/Si. Effect of a change in (a) aspect ratio (diameter/height), (b) particle density, (c) oxide shell thickness. In the last two cases, a hemispherical shape was used. An *ad hoc* broadening was included to match with experimental widths (see Section 2. Simulations have been performed at constant mass except in Figure c and without particle-particle coupling except in Figure b).

signal/noise ratio, a clear transition between growth and early coalescence regimes is observed. Coalescence is characterized by a linear evolution of A_r with thickness, the slope of which depends on growth conditions. At all stages of growth, the larger $\mathcal{A}_s(t) \propto A_r$ signal clearly evidences a better nanoparticle wetting when O_2 is added to the gas flow but also a lack of drastic impact of substrate cleaning by the plasma.

3.5 Ag nanoparticle TEM imaging

Finally, in order to clarify the main impact of O_2 on Ag wetting during the nanoparticle growth stage, films deposited on membranes were imaged by TEM plane views at the same 0.6 nm thickness but at different $\%O_2$ conditions (Figure 12). Such a thickness ensures a deposit in the growth stage at the saturation density sufficiently far from generalized coalescence (see Figure 10-c). Image analysis led to a non-linear increase of particle density ρ_s (Figure 12) with a nearly constant lateral size around 2 nm. Unfortunately, at the opposite to nanoparticle density, uncertainties in deposited thickness and modification of particle shape by encapsulation do not allow to comment reliably the evolution of aspect ratio from mass conservation.

4 Discussion

Based on all the results described in the previous section, the effect of O_2 addition can be separated schematically into three regimes, in terms of O_2 flow during deposition: (i) a *low regime* (for $\%O_2$ between 0 and 4%), (ii) an *intermediate regime* (for $\%O_2$ between 10 and 20%), and (iii) a *high regime* (for $\%O_2$ higher than 20%).

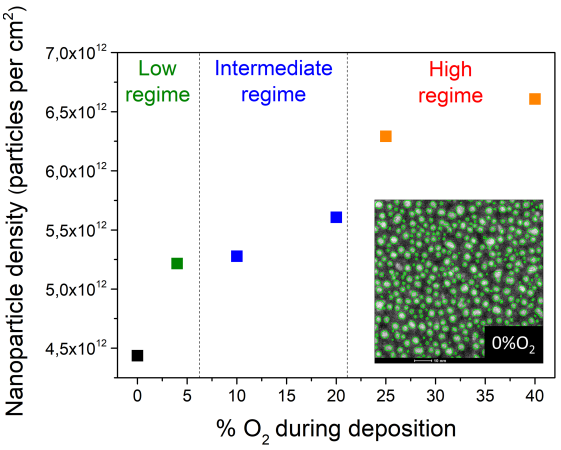

Figure 12: Particle density as obtained from TEM image analysis of 0.6 nm-thick films grown under different $\%O_2$. The inset shows an example of an image (90×90 nm^2) of a film deposited under pure Ar gas after image analysis with the corresponding segmented particles.

4.1 The low $\%O_2$ regime: $0 \leq \%O_2 \leq 4$

In this regime, a sizable 20 % decrease of the percolation threshold t_p (Figure 2) is observed (from 5.5 nm at $0\%O_2$ to 4.3 nm at $4\%O_2$), without a significant impact on the final resistivity at $t = 20$ nm (Figure 2) despite a slight film crystallinity worsening (Figure 9 and Figure S8). Regarding film composition, no clear trace of oxidation in the Ag 3d core level peak is present whatever the thickness within the sensitivity of photoemission spectroscopy (Figure 5), in agreement with previous reports.[10,15] The same conclusion is reached with the low intensity O 1s peak leading to a AgO_x stoichiometry of only $x = 0.02$. If for a 20 nm thick percolated film the major species are the O_β moiety (*i.e.* subsurface oxygen) and its companion surface $O_{\alpha 3}$ moiety (Figure 4-a), the $O_{\alpha 1}$ goes through a maximum at ~ 12 nm in thickness (Figure 6-a). This behaviour, observed even at higher $\%O_2$ (Figure 6-b,c) seems to be related, within the probing depth of photoemission, to the percolation of the film and the fraction of film surface available for $O_{\alpha 1}$ adsorption or for oxidation (Ag_2O). Most likely, $O_{\alpha 3}$-O_β moities are related to the enhanced reactivity of undercoordinated sites present in

nanoparticles with molecular oxygen;[36] indeed, their respective O 1s peaks also appear after exposure of an Ag film grown under pure Ar (Figure S3 and Figure 8) to O_2 gas without plasma.

Based on the present data, different explanations can be put forward for the decrease in percolation threshold in the low $\%O_2$ regime. The first one is an increase in nucleation density.[7,18] Due to the 3D morphology, denser but smaller islands could in principle form a percolated network at a lower deposited thickness than less numerous but larger islands. Assuming that t_p scales with the coalescence threshold t_c, at which impingement between islands occurs, one finds: $t_p \propto t_c \propto D_c^3 \rho_s / A_r$, where ρ_s is the saturation particle density during growth stage, A_r the equilibrium aspect ratio of particles (diameter/height) and D_c the in-plane size of particles at coalescence start. Since particles are in contact with each other at coalescence, $D_c \propto \rho_s^{1/2}$ so that $t_p \propto 1/(\rho_s^{1/2} A_r)$. Thus, any variation of A_r or ρ_s translates into a variation of t_p as:

$$\frac{\Delta t_p}{t_p} = -\frac{\Delta A_r}{A_r} - \frac{1}{2}\frac{\Delta \rho_s}{\rho_s}. \qquad (3)$$

However, TEM experiments (Figure 12) only show a moderate increase of $\sim$ 10 % of the particle density (from $4.4\,10^{12}$ cm^{-2} to $4.9\,10^{12}$ cm^{-2}) when introducing $4\%O_2$, which should give rise to a modest decrease of ~ 5 % for t_p. This value is far from the observed decrease in t_p (-20 %; Figure 2). In addition to this, a larger density of particles should induce an increased grain boundary density in the percolated film and a larger film resistivity, a fact which is not observed experimentally (Figure 2). Thus, a change in nucleation density fails to fully explain the observed drastic decrease in t_p.

The second explanation is an improved wetting of Ag islands in the initial stage of film growth, before coalescence. Flattened particles covering a larger fraction of the substrate surface should impinge on each other at a lower deposited thickness. As shown in Figure 10-c, despite noise in the measurement, the initial value of $\mathcal{A}_s$ and therefore the initial A_r in the growth regime before coalescence, is larger when O_2 is added. This particle flattening effect is also clearly evidenced in the SDRS spectra (Figure 10-a) by the red-shift and increase in intensity of the parallel plasmon peak[47] between $0\%O_2$ and $4\%O_2$ at $t = 0.6$ nm. According to $\mathcal{A}_s(t)$ evolution (Figure 10-c), at such an equivalent thickness, the film is indeed in the growth regime of isolated islands. The trend is consistent with the qualitative simulations shown in Figure 11-a, while the change in particle density through particle-particle electrostatic coupling (Figure 11-b) fails to account for the order of magnitude of the experimental red-shift of the parallel plasmon peak. Moreover, as it will be shown below for the high $\%O_2$ regime, a similar change in particle density is not always correlated with an earlier percolation threshold. Particle flattening may be approached using thermodynamics through surface/interface energy considerations. For a truncated sphere equilibrium shape (*i.e.* ignoring crystalline anisotropy), the contact angle θ_c is driven by the balance between the particle surface energy γ_m, the substrate surface energy γ_s and the interface energy between the two materials γ_i via the Young-Dupré equation:

$$\begin{aligned} W_a &= \gamma_m(1+\cos\theta_c) \\ W_a &= \gamma_s + \gamma_m - \gamma_i, \end{aligned} \qquad (4)$$

where W_a stands for the adhesion energy. The variation ΔA_r of aspect ratio:

$$A_r = \frac{2}{1-\cos\theta_c} \qquad (5)$$

induced by a change in contact angle $\Delta\theta_c$ reads:

$$\frac{\Delta A_r}{A_r} = -\frac{\sin\theta_c \Delta\theta_c}{1-\cos\theta_c}. \qquad (6)$$

Thus, starting from a contact angle of $\theta_c \simeq 130°$, corresponding to the energetics of Ag/SiO_2,[47,67] a change in $\frac{\Delta t_p}{t_p} \simeq -20$ % due to $4\%O_2$ addition (Figure 2) would require a moderate change in $\Delta\theta_c \simeq -24°$ according to

Equation 3 and ignoring the effect of density. Although not directly comparable in terms of temperature, this order of magnitude matches the variation of $\Delta\theta_c \simeq -20°$ observed in the low regime of oxygen activity on melted Ag sessile drop measurements.[17] On a energetic point of view, this would require a variation of:

$$\frac{\Delta W_a}{W_a} - \frac{\Delta\gamma_m}{\gamma_m} = -\frac{\sin\theta_c \Delta\theta_c}{1+\cos\theta_c} \simeq 90\% \qquad (7)$$

which can be achieved by a decrease of γ_m and/or an increase of W_a. This change in interface energetics W_a could be related to the impact of activated O species on the substrate itself, as seen in Figure 7 with the decrease of the C 1s fingerprint of carbonaceous contamination. Even if a slight increase of A_r is observed in the initial value of $\mathcal{A}_s(t)$ after plasma treatment, neither t_p (5.3 nm for a $0\%O_2$ growth on a plasma-treated wafer instead of 5.4 nm for an as-introduced one), nor the slope of evolution of $\mathcal{A}_s(t)$ in the coalescence regime (Figure 10-c), nor the parallel plasmon peak (Figure S9) at $t = 1$ nm are impacted by surface plasma treatment before deposition. All these findings rule out a major impact on Ag wetting of a plasma treatment of the substrate. This contradicts previous findings on ZnO[21,22] but the chemistry of the present substrate is completely different. On the other hand, as previously found by first-principles calculations,[4,18,68,69] the decrease of surface energy due to surface oxygen species is a likely explanation of an enhanced wetting for nanoparticles. Nevertheless, the thermodynamic stability diagrams of O-adsorption at the surface/subsurface of Ag(111)[68] and Ag(100)[69] obtained by *ab initio* calculations show that a variation of surface energy $\frac{\Delta\gamma_m}{\gamma_m}$ of at best -40% can be achieved at the highest oxygen chemical potential, before the formation of bulk Ag_2O. This value is less than half of what is required by Equation 7. At last, due to the overwhelming O 1s signal from the substrate, it is hard to detect in photoemission any specific signature of O segregated at the interface with the substrate. Nevertheless, such interfacial species could lead to a sizeable change in adhesion energy as already pointed out for films deposited in similar oxidative conditions[4,18,21] or upon O_2 adsorption on macroscopic sessile drops.[17]

Lastly, a delay in coalescence dynamics induced by oxygen adsorption could also explain the formation of elongated and irregular-shaped clusters instead of round-shaped islands and therefore an earlier percolation (Figure 2). Previously reported in the literature only via *ex situ* scanning electron microscopy imaging,[18,20] the phenomenon of partial coalescence appears clearly herein, when comparing $0\%O_2$ and $4\%O_2$, in the change in slope in the evolution of $\mathcal{A}_s(t)$ (Figure 10-c) and the match between the experimental ($t = 3$ nm; Figure 10-b) and simulated (Figure 11-a) SDRS line shapes. A likely explanation lies in the observed switch of film texture from 70 % [111]-oriented to 65% [100]-oriented grains when O_2 is introduced in the plasma, as shown in the inset of Figure 9. Besides adsorbed O, the vertical interplanar distance mismatch between [111] (2.35 Å) and [100] (2.045 Å) oriented grains hinders the coalescence process. At $4\%O_2$, this structural impediment reaches a maximum with a 50-50% balance between the two types of grains, not speaking about their random relative in-plane orientations. As predicted by first-principle calculations, such a reversal of film texture could find its origin (i) in a more favourable isolated oxygen adsorption energy at a (100) rather than a (111) surface, associated to a much larger O surface diffusion barrier[70] ; and (ii) in a lower O-covered surface energy of (100)[69] than (111)[68] surface at all O chemical potentials, which nearly compensates the difference in compacity between the two orientations.

To conclude, the earlier percolation induced by the $4\%O_2$ addition results from a combination of effects: (i) change in particle density, (ii) a better wetting before coalescence and (iii) a delayed coalescence due to oxygen adsorption. The last two mechanisms (and not really the substrate cleaning by the plasma) appear to be the most effective. The present measurements do not allow discussing further neither the spillover mechanism or the O interfacial segregation, which were suggested by *ab*

initio calculations.[18,21–23] Nevertheless, the lack of clear-cut oxidation and the presence of only surface/subsurface O moities argue in favour of a "surfactant" mechanism.

4.2 The intermediate $\%O_2$ regime: $10 \leq \%O_2 < 20$

While still being well below the measured value under pure Ar, the thickness at the percolation threshold only slightly decreases from 4 $\%O_2$ to 10-20$\%O_2$ (Figure 2). Concurrently, the resistivity at $t = 20$ nm starts rising (Figure 2). Particle flattening and delayed coalescence are still at work just like in the low $\%O_2$ regime (Figure 10), alongside the effect of particle density increase, although more moderate than in the low O_2 regime (Figure 12).

Chemical analyses in the intermediate regime show a transition towards a component dominated by O_{α_1} species in 20 nm-thick film (Figure 4). In parallel, the fractions x and y of oxidized Ag slowly increase in this regime, even though the major fraction of the film still remains metallic (Figure 4). Following this uptake in O_{α_1} that denotes a more "oxidative" plasma,[36] a gradient of composition develops across the film thickness before reaching a plateau value of $\simeq 8 - 10\%$ at 10 nm (Figure 5-b). In parallel, at intermediate thicknesses (~ 6 nm; Figure 6-b), a Ag_2O (or O_{α_2}) species is detected before completely vanishing in thicker films. These observations can be linked to a change in the oxidation behaviour of the exposed Ag surface that follows the growth mode of the film *i.e.* the transition from 3D particles to a continuous and uniform film. The case being clearer in high $\%O_2$ regime, it will be commented in the next section.

Optical spectra at $t = 0.6$ nm (Figure 10-a) for 10$\%O_2$ start differing from those corresponding to 4 $\%O_2$. The trend becomes clearer (Figure 10-b) at $t = 3$ nm, with an overall decrease in intensity and a red-shift of both resonances. According to dielectric simulations (Figure 11-c), these observations can be explained by the formation of a core-shell structure due to adsorbed oxygen. A similar trend is observed later in the high $\%O_2$ regime at 40$\%O_2$ (see below). Thus, the initial stage of deposition is mainly governed by the growth of metallic nanoparticles with absorbed O at their surface in a core-shell like-configuration that is the starting point for the gradual oxidation of the film with increasing thickness.

4.3 The high $\%O_2$ regime: $\%O_2 \geq 20$

The high $\%O_2$ regime is characterized by an abrupt increase of the oxide fraction AgO_x in the film stoichiometry at $t = 20$ nm (Figure 4-b), which stabilizes at $x = 0.26$ for 40$\%O_2$, a value only slightly lower than for a deposition under pure O_2 ($x = 0.28$). From the Ag 3d core level, all Ag atoms appear to be in an oxidized state (Figure 4-a) at $t = 20$ nm. This goes with a drastic change in film chemistry; above 20$\%O_2$ at $t = 20$ nm, the O 1s core level is characteristic of an Ag_2O-like compound (Figure 4-a). Therefore, in agreement with previous reports,[15] thick films deposited in the high O_2 regime appear to be mainly composed of a highly sub-stoichiometric oxide that is not crystallized (see Figure 9).

Both the percolation threshold and the film resistivity at $t = 20$ nm (Figure 2) follow a linear evolution from the intermediate regime. The increase in resistivity is consistent with the enhanced film oxidation, but also with the increase in nanoparticle density (Figure 12) that scales with the final grain boundary density in the percolated film. However, compared to resistivity expected for a pure oxide (59.3 Ω.cm for AgO and $3.3\,10^3 - 7\,10^8$ Ω.cm for Ag_2O),[13,16,38] the seven order of magnitude lower value measured at 40$\%O_2$ (57 $\mu\Omega$.cm) suggests that the $t = 20$ nm thick film is not homogeneous. This composition gradient across the layer appears in the photoemission analysis (Figure 5-b,c).

Besides resistivity, SDRS and XRD measurements also raise the question of composition gradient in the film. Metal particles are re-

quired to observe a plasmon resonance at low thickness (Figure 10-a). At the start of deposition in the nanoparticle growth regime, the film is mostly metallic according to photoemission (Figure 5-c), thus explaining the presence of Ag metal peaks in $t = 20$ nm XRD patterns (Figure 9). These nanoparticles form through competitive mechanisms of metal-metal clustering by fast Ag surface diffusion on silica and of oxidation, probably mainly by direct impact as the substrate itself reacts with activated-oxygen species (Figure 7). As the surface coverage increases, they further oxidize. Thus, the optical signature for the formation of an oxide shell on a metallic core (red shift for the parallel plasmon peak alongside a decrease in intensity) is even more apparent in SDRS spectra at higher thickness values (Figure 11-b at $t = 3$ nm versus Figure 11-a at $t = 0.6$ nm). After percolation, and moreso after the formation of a continuous film, the oxide fraction reaches about half of its final value (Figure 5-b; 40%O_2; $t > 6$ nm). In this thickness regime, film growth takes place on a Ag-suboxide where Ag ad-atom diffusion is slowed down, and metallic Ag clustering is unlikely compared to SiO_2, given its higher adsorption energy. Moreover, the sticking coefficient of activated O species,[15] and probably their diffusion lengths at the surface, increase. Thus, a change from an oxidation mechanism of "Eley-Rideal" to a "Langmuir-Hinshelwood" type due to the evolution of the film morphology leads to an oxidation gradient with (mostly) metallic Ag being deposited in the initial stages. This explains (i) the existence of an initial plasmonic signal (Figure 10-a), (ii) a reflectivity characteristic of a percolated film at $t = 3$ nm with a continuous increase in the near infrared, (iii) a low resistivity of the final film compared to a bulk oxide and (iv) the presence of Ag metallic XRD reflections albeit less crystalline for higher %O_2 conditions. The transition and the actual oxidation state of the film is governed by the balance between (i) the fraction of covered substrate (and thus the film morphology), (ii) the relative arrival rates of Ag and activated O species and (iii) their relative sticking coefficients and diffusion lengths on SiO_2 and Ag-suboxide. This existence of the initial competition between metal clustering and oxidation is confirmed by the strong reactivity observed during post-growth exposure to a O-rich plasma (20%O_2 in Figure 8); in principle, complete Ag oxidation is not really impeded. On the other hand, the growth under pure O_2 plasma is not even able to reach a stoichiometry close to Ag_2O ($x = 0.28$). Anticipated in the previous section, such a general scenario seems to be also at work also in the intermediate regime of %O_2, but to a lesser extent, as the content of activated species in the plasma is lower (Figure 5). The transition from metallic to more oxidized Ag (Figure 5) and the switch from $O_{\alpha 3}$-O_β [probably related to molecular O_2 adsorption (Figure S3 and Figure 8)] to Ag_2O moities (Figure 6) correlate with the percolation threshold of the film.

All these observations rationalise the methodology of gas deployment in the early stage of growth proposed in previous studies[9,10,12] to benefit from earlier film percolation while avoid the deleterious impact of oxidation on film resistivity. But such trick is not the panacea; it requires an apparatus-dependent optimisation as it relies on a subtle kinetic balance between growth and oxidation rates.

5 Conclusion

The effect of O_2 addition during sputter deposition of Ag films was investigated using a combination of *in situ* and real-time techniques. Photoemission, resistivity and plasmonics evidenced three distinct regimes. Firstly, at low O_2 flow ($0 \leq$ %$O_2 \leq 4$), a combined effect of (i) nanoparticle flattening and density increase in the initial stages of film growth, (ii) a delayed coalescence and (iii) a change in film texture from [111] to [100] can explain the strong reduction in the percolation threshold thickness. Neither clear-cut Ag oxidation nor film resistivity increase are observed. The observed change in surface/interface energy due to the formation of adsorbed $O_{\alpha 1}/O_{\alpha 3}$ and subsurface O_β moities on the growing nanoparticles was put forward to explain these findings. In the intermediate

regime ($10 \leq \%O_2 < 20$), in addition to the particle flattening, to the onset of increase in resistivity and to a weaker decrease in percolation threshold thickness, $O_{\alpha 1}$ moieties become the main species of adsorbed oxygen. Finally, in the high regime ($\%O_2 \geq 20$), actual oxidation takes places in the form of an Ag_2O-like amorphous/not-crystallized compound and has a strong impact on resistivity. In all regimes, a composition gradient is observed with mostly metallic silver at the interface with the substrate and an enrichment in O close to the film surface. In parallel to the thermodynamically-favoured O segregation to the surface, a kinetic explanation was proposed based on a change in the oxidation mechanism depending on the nature of the surface (SiO_2 then AgO_x) on which Ag atoms are landing and the oxidative character of the plasma. This transition results from a complex balance between substrate reactivity, arrival rates of Ag and of activated O species, metal-metal aggregation, O diffusion and film morphology. In this respect, the use of *in situ* and real-time techniques turned out to be quite relevant in clarifying the interplay between chemistry, morphology and structure in the growth modifier effect of O_2. In addition, they can provide an opportunity to follow ageing effect related to film chemical[23] or morphological instabilities.

Supporting Information Available

Set of XPS, SDRS and XRD complementary figures cited in the text.

Acknowledgement R.Z. would like to thank Saint-Gobain Research Paris and ANRT (Agence Nationale Recherche Technologie) for his PhD funding and M.-C. Solignac (SVI) for valuable discussions about SDRS. L. Largeau (C2N, France) is acknowledged for his help during TEM experiments.

References

(1) Zhao, G.; Wang, W.; Bae, T.-S.; Lee, S.-G.; Mun, C.; Lee, S.; Yu, H.; Lee, G.-H.; Song, M.; Yun, J. Stable Ultrathin Partially Oxidized Copper Film Electrode for Highly Efficient Flexible Solar Cells. *Nature Communications* **2015**, *6*, 8830.

(2) Rezaei, S. D.; Shannigrahi, S.; Ramakrishna, S. A Review of Conventional, Advanced, and Smart Glazing Technologies and Materials for Improving Indoor Environment. *Solar Energy Materials & Solar Cells* **2017**, *159*, 26 – 51.

(3) Messaykeh, M.; Chenot, S.; David, P.; Cabailh, G.; Jupille, J.; Koltsov, A.; Lazzari, R. An in Situ and Real-Time Plasmonic Approach of Seed/adhesion Layers: Chromium Buffer Effect at the Zinc/alumina Interface. *Crystal Growth Design* **2021**, *21*, 3528–3539.

(4) Zhao, G.; Shen, W.; Jeong, E.; Lee, S.-G.; Yu, S. M.; Bae, T.-S.; Lee, G.-H.; Han, S. Z.; Tang, J.; Choi, E.-A.; Yun, J. Ultrathin Silver Film Electrodes with Ultralow Optical and Electrical Losses for Flexible Organic Photovoltaics. *ACS Applied Materials & Interfaces* **2018**, *10*, 27510–27520.

(5) Egelhoff, W. F.; Steigerwald, D. A. The Role of Adsorbed Gases in Metal on Metal Epitaxy. *Journal of Vacuum Science and Technology A* **1989**, *7*, 2167–2173.

(6) Riveiro, J. M.; Normile, P. S.; Andrés, J. P.; Gonzalez, J. A.; De Toro, J. A.; Muñoz, T.; Muñiz, P. Oxygen-Assisted Control of Surface Morphology in Nonepitaxial Sputter Growth of Ag. *Applied Physics Letters* **2006**, *89*, 201902.

(7) Wang, W.; Song, M.; Bae, T.-S.; Park, Y. H.; Kang, Y.-C.; Lee, S.-G.; Kim, S.-Y.; Kim, D. H.; Lee, S.; Min, G.; Lee, G.-H.; Kang, J.-W.; Yun, J. Transparent Ultrathin Oxygen-Doped Silver Electrodes for Flexible Organic So-

lar Cells. *Advanced Functional Materials* **2014**, *24*, 1551–1561.

(8) Yun, J.; Wang, W.; Bae, T. S.; Park, Y. H.; Kang, Y. C.; Kim, D. H.; Lee, S.; Lee, G. H.; Song, M.; Kang, J. W. Preparation of Flexible Organic Solar Cells with Highly Conductive and Transparent Metal-Oxide Multilayer Electrodes Based on Silver Oxide. *ACS Applied Materials and Interfaces* **2013**, *5*, 9933–9941.

(9) Pliatsikas, N.; Jamnig, A.; Konpan, M.; Delimitis, A.; Abadias, G.; Sarakinos, K. Manipulation of Thin Silver Film Growth on Weakly Interacting Silicon Dioxide Substrates Using Oxygen As a Surfactant. *Journal of Vacuum Science & Technology A* **2020**, *38*, 0734–2101.

(10) Jamnig, A.; Pliatsikas, N.; Konpan, M.; Lu, J.; Kehagias, T.; Kotanidis, A. N.; Kalfagiannis, N.; Bellas, D. V.; Lidorikis, E.; Kovac, J.; Abadias, G.; Petrov, I.; Greene, J. E.; Sarakinos, K. 3D-to-2D Morphology Manipulation of Sputter-Deposited Nanoscale Silver Films on Weakly Interacting Substrates Via Selective Nitrogen Deployment for Multifunctional Metal Contacts. *ACS Appl Nano Mater* **2020**, *3*, 4728–4738.

(11) Yun, J.; Chung, H. S.; Lee, S. G.; Bae, J. S.; Hong, T. E.; Takahashi, K.; Yu, S. M.; Park, J.; Guo, Q.; Lee, G.-H.; Han, S. Z.; Ikoma, Y.; Choi, E.-A. An Unexpected Surfactant Role of Immiscible Nitrogen in the Structural Development of Silver Nanoparticles: An Experimental and Numerical Investigation. *Nanoscale* **2020**, *12*, 1749–1758.

(12) Zhao, G.; Jeong, E.; Lee, S.-G.; Yu, S. M.; Bae, J.-S.; Rha, J.; Lee, G.-H.; Ikoma, Y.; Yun, J. Insights into Effects of O-Incorporated Ag Nanoparticles As Wetting Seeds toward Improving Ag Wetting on Oxides. *Applied Surface Science* **2021**, *562*, 150135.

(13) Abe, Y.; Hasegawa, T.; Kawamura, M.; Sasaki, K. Characterization of Ag Oxide Thin Films Prepared by Reactive RF Sputtering. *Vacuum* **2004**, *76*, 1–6.

(14) Kim, W.; Ku, D.; Lee, K.; Cheong, B. Effect of Oxygen Content and Deposition Temperature on the Characteristics of Thin Silver Films Deposited by Magnetron Sputtering. *Applied Surface Science* **2010**, *257*, 1331–1336.

(15) Snyders, R.; Wautelet, M.; Gouttebaron, R.; Dauchot, J.; Hecq, M. Experimental and Theoretical Studies of the DC Reactive Magnetron Sputtering Deposition of Silver Oxide Thin Films. *Surface and Coatings Technology* **2003**, *174-175*, 1282–1286.

(16) Pierson, J. F.; Wiederkehr, D.; Billard, A. Reactive Magnetron Sputtering of Copper, Silver, and Gold. *Thin Solid Films* **2005**, *478*, 196–205.

(17) Chatain, D.; Chabert, F.; Ghetta, V.; Fouletier, J. New Experimental Setup for Wettability Characterization under Monitored Oxygen Activity : II Wettability of Sapphire by Silver-Oxygen Melts. *Journal of the American Ceramic Society* **1994**, *77*, 197–201.

(18) Zhao, G. Q.; Jeong, E.; Choi, E. A.; Yu, S. M.; Bae, J. S.; Lee, S. G.; Han, S. Z.; Lee, G. H.; Yun, J. Strategy for Improving Ag Wetting on Oxides: Coalescence Dynamics Versus Nucleation Density. *Applied Surface Science* **2020**, *510*, 145515.

(19) Grachev, S.; De Grazia, M.; Barthel, E.; Søndergård, E.; Lazzari, R. Real Time Monitoring of Nanoparticle Film Growth at High Deposition Rate with Optical Spectroscopy of Plasmon Resonances. *Journal of Physics D: Applied Physics* **2013**, *46*, 375305–375315.

(20) Jeong, E.; Lee, S.-G.; Bae, J.-S.; Yu, S. M.; Han, S. Z.; Lee, G.-H.; Choi, E.-A.;

Yun, J. Effects of Substantial Atomic-Oxygen Migration across Silver-Oxide Interfaces during Silver Growth. *Applied Surface Science* **2021**, *568*, 150927.

(21) Jeong, E.; Lee, S.-G.; Yu, S. M.; Bae, J.-S.; Han, S. Z.; Lee, G.-H.; Choi, E.-A.; Yun, J. Dependency of Ag Wetting on the Oxygen Nonstoichiometry of Oxide Surfaces. *Appl Surf Sci* **2023**, *611*, 155699.

(22) Jeong, E.; Ikoma, Y.; Yu, S. M.; Bae, J.-S.; Lee, S.-G.; Han, S. Z.; Lee, G.-H.; Chae, W.-S.; Choi, E.-A.; Yun, J. Nonconventional Nucleation and Growth of Au Nanoparticles with Improved Adhesion on Oxygen-Excessive Oxide Surfaces. *Appl. Surf. Sci.* **2021**, *553*, 149385.

(23) Jeong, E.; Lee, S.-G.; Yu, S. M.; Han, S. Z.; Lee, G.-H.; Ikoma, Y.; Choi, E.-A.; Yun, J. Spontaneous Post-Growth Oxygen Dissipation and Electrical Improvement of Silver Electrodes in Substoichiometric Oxidation States. *Appl Surf Sci* **2023**, *623*, 156998.

(24) Weaver, J. F.; Hoflund, G. B. Surface Characterization Study of the Thermal Decomposition of Ag_2O. *Chemistry of Materials* **1994**, *6*, 1693–1699.

(25) Epling, W. S.; Hoflund, G. B.; Salaita, G. N. Surface Characterization Study of the Thermal Decomposition of Ag_2CO_3. *The Journal of Physical Chemistry B* **1998**, *102*, 2263–2268.

(26) Pierson, J. F.; Rousselot, C. Stability of Reactively Sputtered Silver Oxide Films. *Surface and Coatings Technology* **2005**, *200*, 276–279.

(27) Schön, G. ESCA Studies of Ag, Ag_2O and AgO. *Acta Chemica Scandinavia* **1973**, *27*, 2623–2633.

(28) Hammond, J. S.; Gaarenstroom, S. W.; Winograd, N. X-Ray Photoelectron Spectroscopic Studies of Cadmium- and Silver-Oxygen Surfaces. *Analytical Chemistry* **1975**, *47*, 2193–2199.

(29) Kaushik, V. K. XPS Core Level Spectra and Auger Parameters for Some Silver Compounds. *Journal of Electron Spectroscopy and Related Phenomena* **1991**, *56*, 273–277.

(30) Bao, X.; Muhler, M.; Schedel-Niedrig, T.; Schlögl, R. Interaction of Oxygen with Silver at High Temperature and Atmospheric Pressure: A Spectroscopic and Structural Analysis of a Strongly Bound Surface Species. *Physical Review B* **1996**, *54*, 2249–2262.

(31) Tjeng, L. H.; Meinders, M. B. J.; van Elp, J.; Ghijsen, J.; Sawatzky, G. A.; Johnson, R. L. Electronic Structure of Ag_2O. *Physical Review B* **1990**, *41*, 3190–3199.

(32) Hoflund, G. B.; Hazos, Z. F.; Salaita, G. N. Surface Characterization Study of Ag, AgO, and Ag_2O Using X-Ray Photoelectron Spectroscopy and Electron Energy-Loss Spectroscopy. *Physical Review B* **2000**, *62*, 11126–11133.

(33) Waterhouse, G. I. N.; Bowmaker, G. A.; Metson, J. B. Oxidation of a Polycrystalline Silver Foil by Reaction with Ozone. *Applied Surface Science* **2001**, *183*, 191–204.

(34) Bielmann, M.; Schwaller, P.; Ruffieux, P.; Gröning, O.; Schlapbach, L.; Gröning, P. AgO Investigated by Photoelectron Spectroscopy: Evidence for Mixed Valence. *Physical Review B* **2002**, *65*, 235431.

(35) Kaspar, T. C.; Droubay, T.; Chambers, S. A.; Bagus, P. S. Spectroscopic Evidence for Ag(III) in Highly Oxidized Silver Films by X-Ray Photoelectron Spectroscopy. *The Journal of Physical Chemistry C* **2010**, *114*, 21562–21571.

(36) Rocha, T. C. R.; Oestereich, A.; Demidov, D. V.; Hävecker, M.; Zafeiratos, S.; Weinberg, G.; Bukhtiyarov, V. I.; Knop-Gericke, A.; Schlögl, R. The Silver–Oxygen System in Catalysis: New

Insights by near Ambient Pressure X-Ray Photoelectron Spectroscopy. *Physical Chemistry Chemical Physics* **2012**, *14*, 4554–4564.

(37) Rehren, C.; Muhler, M.; Bao, X.; Schlögl, R.; Ertl, C. The Interaction of Silver with Oxygen. *Zeitschrift für Physikalische Chemie* **1991**, *174*, 11 – 52.

(38) Rivers, S. B.; Bernhardt, G.; Wright, M. W.; Frankel, D. J.; Steeves, M. M.; Lad, R. J. Structure, Conductivity, and Optical Absorption of Ag_2O_x Films. *Thin Solid Films* **2007**, *515*, 8684–8688.

(39) Lazzari, R. `Igor Pro Paris Photoemission Package` can be downloaded with a user guide from: http://www.insp.upmc.fr/I4P-Igor-Pro-Paris-Photoemission.html?lang=en.

(40) Moulder, J. F.; Stickle, W. F.; Sobol, P. E.; Bomben, K. D. In *Handbook of X-Ray Photoelectron Spectroscopy*; Chastian, J., King, R. C. J., Eds.; Physical Electronics, Perkin Elmer.: Eden Prairie, Minnesota, USA, 1995.

(41) Guilet, S.; Bataillou, L.; Kerivel, O.; Lazzari, R. Determination of the Intensity/energy Response Function of an Hemispherical Photoelectron Analyser Based on Tougaard Background. *Journal of Electron Spectroscopy and Related Phenomena* **2022**, *258*, 147225.

(42) Salaita, G. N.; Hazos, Z. F.; Hoflund, G. B. Surface Characterization Study of the Thermal Decomposition of Ag_2CO_3 Using X-Ray Photoelectron Spectroscopy and Electron Energy Loss Spectroscopy. *Journal of Electron Spectroscopy and Related Phenomena* **2000**, *107*, 73–81.

(43) Miccoli, I.; Edler, F.; Pfnür, H.; Tegenkamp, C. The 100th Anniversary of the Four-Point Probe Technique: The Role of Probe Geometries in Isotropic and Anisotropic Systems. *Journal of Physics: Condensed Matter* **2015**, *27*, 223201.

(44) Rycroft, I. M.; Evans, B. L. The *In Situ* Characterization of Metal Film Resistance during Deposition. *Thin Solid Films* **1996**, *290-291*, 283 – 288.

(45) Lazzari, R.; Jupille, J.; Cavallotti, R.; Simonsen, I. Model-Free Unraveling of Supported Nanoparticles Plasmon Resonance Modes. *The Journal of Physical Chemistry C* **2014**, *118*, 7032–7048.

(46) Gozhyk, I.; Dai, L.; Hérault, Q.; Lazzari, R.; Grachev, S. Plasma Emission Correction in Reflectivity Spectroscopy during Sputtering Deposition. *Journal of Physics D: Applied Physics* **2018**, *52*, 095202.

(47) Lazzari, R.; Jupille, J.; Cavallotti, R.; Chernysheva, E.; Castilla, S.; Messaykeh, M.; Hérault, Q.; Gozhyk, I.; Meriggio, E. Plasmonics of Supported Nanoparticles Reveals Adhesion at the Nanoscale: Implications for Metals on Dielectrics. *ACS Applied Nano Materials* **2020**, *3*, 12157–12168.

(48) Lazzari, R.; Simonsen, I. GranFilm: A Software for Calculating Thin-Layer Dielectric Properties and Fresnel Coefficients. *Thin Solid Films* **2002**, *419*, 124–136.

(49) Bedeaux, D.; Vlieger, J. *Optical Properties of Surfaces*; Imperial College Press: London, 2001.

(50) Indrehus, S. Plasmonics Properties of Supported Nanoparticles. Ph.D. thesis, Sorbonne University, 2020.

(51) Palik, E. D. *Handbook of Optical Constants of Solids*; Academic Press, 1985; Vol. 1-3.

(52) Gao, X.-Y.; Feng, H.-L.; Ma, J.-M.; Zhang, Z.-Y.; Lu, J.-X.; Chen, Y.-S.; Yang, S.-E.; Gu, J.-H. Analysis of the Dielectric Constants of the Ag_2O Film

by Spectroscopic Ellipsometry and Single-Oscillator Model. *Physica B: Condensed Matter* **2010**, *405*, 1922–1926.

(53) Simonsen, I.; Lazzari, R.; Jupille, J.; Roux, S. Numerical Modelling of the Optical Response of Supported Metallic Particles. *Physical Review B* **2000**, *61*, 7722–7733.

(54) Lazzari, R.; Simonsen, I.; Bedeaux, D.; Vlieger, J.; Jupille, J. Polarizability of Truncated Spheroidal Island Supported by a Substrate : Models and Applications. *European Physical Journal B: Condensed Matter and Complex Systems* **2001**, *24*, 267–284.

(55) Lazzari, R.; Jupille, J. Growth Kinetics and Size-Dependent Wetting of Ag/α-Al_2O_3(0001) Nanoparticles Studied Via the Plasmonic Response. *Amber, Resinite, and Fossil Resins* **2012**, *23*, 135707.

(56) Zaumseil, P. High-Resolution Characterization of the Forbidden Si(200) and Si(222) Reflections. *Journal of Applied Crystallography* **2015**, *48*, 528–532.

(57) Grönbeck, S., H.and Klacar; Martin, N. M.; Hellman, A.; Lundgren, E.; Andersen, J. N. Mechanism for Reversed Photoemission Core-Level Shifts of Oxidized Ag. *Physical Review B* **2012**, *85*, 115445.

(58) Suzuki, R. O.; Ogawa, T.; Ono, K. Use of Ozone to Prepare Silver Oxides. *Journal of the American Ceramic Society* **1999**, *82*, 2033–2038.

(59) Campbell, C. T. Atomic and Molecular Oxygen Adsorption on Ag(111). *Surface Science* **1985**, *157*, 43–60.

(60) Pettinger, B.; Bao, X.; Wilcock, I. C.; Muhler, M.; Ertl, G. Surface-Enhanced Raman Scattering from Surface and Subsurface Oxygen Species at Microscopically Well-Defined Ag Surfaces. *Physical Review Letters* **1994**, *72*, 1561–1564.

(61) Rocca, M.; Savio, L.; Vattuone, L.; Burghaus, U.; Palomba, V.; Novelli, N.; Buatier de Mongeot, F.; Valbusa, U.; Gunnella, R.; Comelli, G.; Baraldi, A.; Lizzit, S.; Paolucci, G. Phase Transition of Dissociatively Adsorbed Oxygen on Ag(001). *Physical Review B* **2000**, *61*, 213–227.

(62) Bukhtiyarov, V. I.; Hävecker, M.; Kaichev, V. V.; Knop-Gericke, A.; Mayer, R. W.; Schlögl, R. Atomic Oxygen Species on Silver: Photoelectron Spectroscopy and X-Ray Absorption Studies. *Physical Review B* **2003**, *67*, 235422.

(63) Martin, N. M.; Klacar, S.; Grönbeck, H.; Knudsen, J.; Schnadt, J.; Blomberg, S.; Gustafson, J.; Lundgren, E. High-Coverage Oxygen-Induced Surface Structures on Ag(111). *The Journal of Physical Chemistry C* **2014**, *118*, 15324–15331.

(64) Jones, T. E.; Rocha, T. C. R.; Knop-Gericke, A.; Stampfl, C.; Schlögl, R.; Piccinin, S. Thermodynamic and Spectroscopic Properties of Oxygen on Silver under an Oxygen Atmosphere. *Physical Chemistry Chemical Physics* **2015**, *17*, 9288–9312.

(65) Jeong, E.; Lee, S.-G.; Bae, J.-S.; Yu, S. M.; Mun, C.; Han, S. Z.; Lee, G.-H.; Choi, E.-A.; Yun, J. Establishing Substoichiometric Ag Oxidation and Its Physicochemical, Optoelectrical, and Structural Consequences for Ag Electrodes. *ACS Applied Electronic Materials* **2022**, *4*, 4683–4693.

(66) Lazzari, R.; Roux, S.; Simonsen, I.; Jupille, J.; Bedeaux, D.; Vlieger, J. Multipolar Optical Absorptions in Supported Metallic Particles: The Case of Ag/Al_2O_3(0001). *Physical Review B* **2002**, *65*, 235424–1.

(67) Campbell, C. T. Ultrathin Metal Films and Particles on Oxide Surfaces: Structural, Electronic and Chemisorptive Prop-

erties. *Surface Science Reports* **1997**, *27*, 1–111.

(68) Li, W.-X.; Stampfl, C.; Scheffler, M. Insights into the Function of Silver As an Oxidation Catalyst by *Ab Initio* Atomistic Thermodynamics. *Physical Review B* **2003**, *68*, 165412.

(69) Gajdoš, M.; Eichler, A.; Hafner, J. Ab Initio Density Functional Study of O on the Ag(001) Surface. *Surface Science* **2003**, *531*, 272–286.

(70) Zhu, L.; Xu, H.; Nan, Y.; Zhu, J.; Cheng, D. Facet-Dependent Diffusion of Atomic Oxygen on Ag Surfaces. *Computational Materials Science* **2018**, *155*, 17–27.

Graphical TOC Entry